

20

Energy Collected and Delivered by PV Modules

Eduardo Lorenzo

Instituto de Energía Solar – Universidad Politécnica de Madrid, Madrid, Spain

20.1 INTRODUCTION

This chapter deals with two different questions: “How much solar radiation reaches the surface of a photovoltaic (PV) collector?” and “What is the conversion efficiency of this solar radiation into electricity?” Both questions are analysed from the PV-system designer’s point of view, whose ultimate interests, depending on the type of application, are the determination of the PV collector surface needed to provide a certain required service, and the estimation of the average electricity yield from a certain PV array.

The input information available for the PV designer is usually restricted to the 12 monthly mean values of global horizontal irradiation, that characterise the solar climate of the location, and to the electrical characteristics of the PV modules under Standard Test Conditions (STC), as provided by its manufacturers. This chapter contains a whole set of procedures applicable to most PV engineering practical problems using only this input information. In particular, models to predict the long-term evolution of the solar radiation incident over any arbitrarily oriented surface, and also models to anticipate the electricity output of PV arrays operating in other than STC are described. Looking for practical usefulness, the chapter is, as far as possible, self-contained and the formulae are presented in such a way, that they can be applied directly to practical problems, even if sometimes empirical or cumbersome expressions have to be introduced. Some examples intended to clarify the proper use of the formulae have also been included.

The two above-mentioned questions intrinsically differ in nature. The random character of the solar radiation over the Earth implies that answers to the first question are never more than future predictions, unavoidably associated with a degree of uncertainty (even if very good past solar radiation data are available). This uncertainty is more than is commonly assumed, and represents a serious limit to the accuracy (or, more strictly, to

the significance) of the results of any PV design exercise, irrespective of the complexity of the radiation and PV array models supporting the particular design tool. This means that for stand-alone PV systems, reliability can only be properly estimated for Loss of Load Probabilities greater than 10^{-2} . For grid-connected systems, it implies that yield predictions should be understood to have an uncertainty that can reach up to $\pm 30\%$, for monthly values, and $\pm 10\%$ for annual ones.

Regarding the behaviour of PV modules in arbitrary operating conditions, an $I-V$ model based on the incident irradiance and ambient temperature is presented. Particular attention is paid to the consideration of incidence angle effects, which can be significant in several real situations. Further refinements to incorporate the effects of wind speed, solar spectrum and low irradiance effects are also described. These second-order effects help to explain temporary differences between predicted and observed values, but are of minor importance when long-term energy production calculations are considered.

Finally, some problems related to relevant applications are particularly addressed: the reliability of stand-alone PV systems, the case of Solar Home Systems (SHS) (characterised by a large variety of individual real energy consumption values in contrast to only a few standard ones for design purposes), and the energy yield of grid-connected PV systems.

20.2 MOVEMENT BETWEEN SUN AND EARTH

Although the movement of the sun relative to a fixed point on the Earth seems very familiar, because the sun is fortunately there everyday, the mathematics that governs it is surprisingly complex. In fact, the understanding of such movement was among the longest scientific adventures of mankind. It seems that the very first sundials were built in the Babylonian time (1800 BC), and that the attempts to explain the evolution of the “gnomon” shadow led to the first proposed models of the Sun–Earth movement, which in turn led to the beginning of geometry, in Greece [1]. Figure 20.1 pays a fully

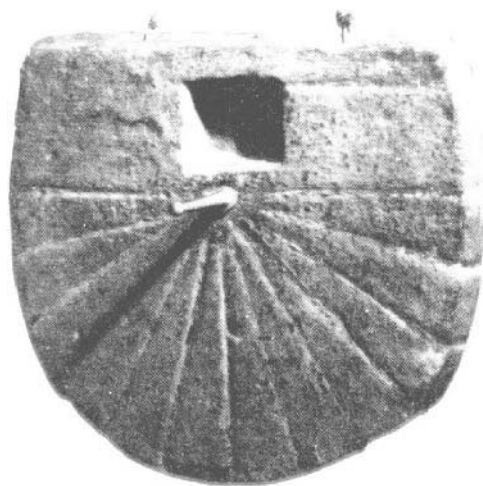


Figure 20.1 Sundial about 2000 years old

deserved homage to such a glorious background. However, it was not until the seventeenth century, when Kepler published *Astronomia Nova* (1609) and *Harmonice mundi* (1618), that such movement was completely explained. And then the explanation spread only very slowly. For example, Galileo in his *Dialogo sopra y due massimi del mundo*, published in 1632 (just one year before the famous ecclesiastic sentence condemning him for publicly defending the heliocentric system formerly proposed by Copernicus), still promoted the idea of the planets revolving around the sun in circular orbits, fully ignoring Kepler's work.

Fortunately for us, such discussions ended a long time ago. Today, it is well established that the Earth goes around the sun in an elliptic orbit with the sun at one of the foci. The plane containing this orbit is called the *ecliptic plane* and the time that the Earth takes to complete this orbit leads to the definition of the year. The distance from the sun to the Earth, r , is given by

$$r = r_0 \left[1 + 0.017 \sin \left(\frac{360(d_n - 93)}{365} \right) \right] \quad (20.1)$$

where d_n is the day number counted from the beginning of the year. It is worth noting that the eccentricity of the ecliptic is only 0.017, that is, very small. Because of that, the deviation of the orbit from the circular is also very small, and it is normally adequate to express the distance just in terms of its mean value r_0 , equal to 1.496×10^8 km, and is usually referred to as *one astronomical unit*, 1 AU. For most engineering applications, a very simple and useful expression for the so-called eccentricity correction factor is

$$\varepsilon_0 = (r_0/r)^2 = 1 + 0.033 \cos \left(\frac{360d_n}{365} \right) \quad (20.2)$$

The Earth also spins once a day on its own central axis, the *polar axis*. The polar axis orbits around the sun, maintaining a constant angle of 23.45° with the ecliptic plane. This inclination is what causes the sun to be higher in the sky in the summer than in the winter. It is also the cause of longer summer sunlight hours and shorter winter sunlight hours. Figure 20.2 shows the Earth's orbit around the sun, with the inclined polar axis; and Figure 20.3 adds some details for a particular day and a particular geographic latitude, ϕ . It is important to note that the angle between the equatorial plane and a straight line drawn between the centre of the Earth and the centre of the sun is constantly changing over the year. This angle is known as the *solar declination*, δ . For our present purposes, it may be considered as approximately constant over the course of any one day. The maximum variation in δ over 24 h is less than 0.5° . If angles north of the equator are considered as positive and south of the equator are considered negative, the solar declination can be found from

$$\delta = 23.45^\circ \sin \left[\frac{360(d_n + 284)}{365} \right] \quad (20.3)$$

On the *spring equinox* (20th/21st March) and the *autumn equinox* (22nd/23rd September), the line between the Sun and the Earth passes through the equator. Consequently, $\delta = 0$, the length of day and night is equal all over the Earth, and the sun rises and sets precisely in the east and west, respectively. On the *summer solstice* (21st/22nd June) $\delta = 23.45^\circ$,

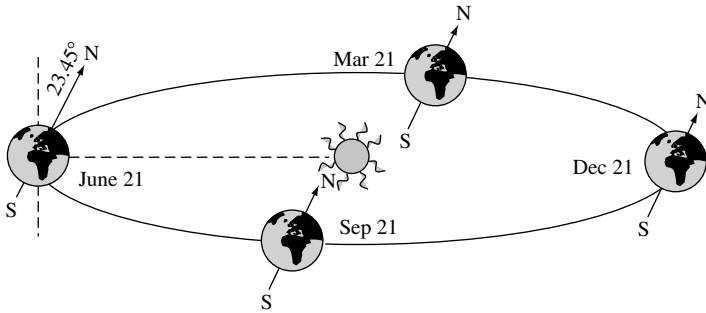


Figure 20.2 The orbit of the Earth around the sun

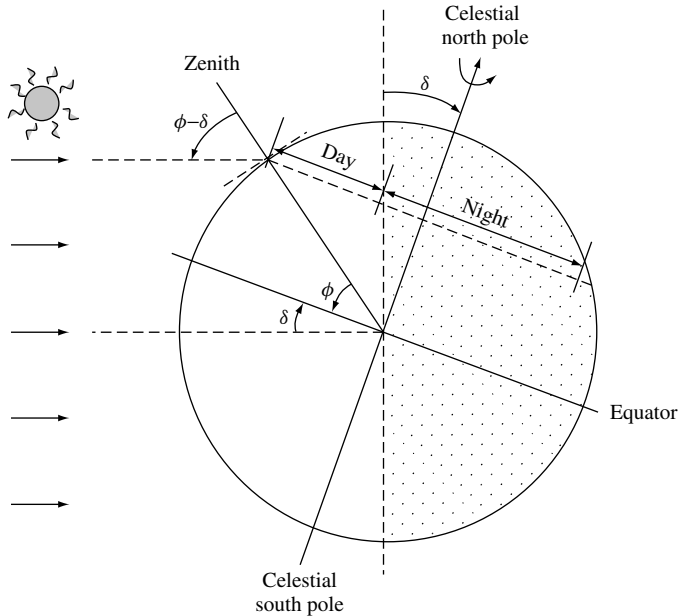


Figure 20.3 Relative Earth–Sun position at noon of a negative declination day (winter in the Northern Hemisphere, and summer in the Southern Hemisphere)

the sun is situated directly above the Tropic of Cancer, and sunrise and sunset are displaced towards the north-east and north-west, respectively. In the Northern Hemisphere, the summer solstice is when the longest day and shortest night of the whole year occur. In the Southern Hemisphere, it is the opposite. On the *winter solstice* (21st/22nd December) $\delta = -23.45^\circ$, the sun is directly above the Tropic of Capricorn, and sunrise and sunset are displaced towards the south-east and south-west, respectively. In the Northern Hemisphere, this is the shortest day and longest night of the whole year, and again, the opposite is true in the Southern Hemisphere.

A classic way of representing the sky is as a sphere centred on a fixed point of the Earth, as indicated in Figure 20.4. This is known as the *celestial sphere*. Each of its

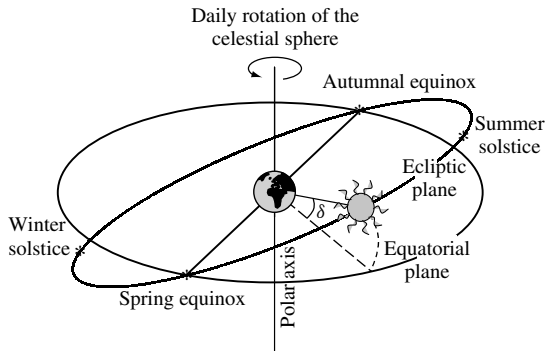


Figure 20.4 The celestial sphere and the ecliptic plane

points represents a direction towards the sky as seen from the Earth. The intersection of the celestial sphere with the equatorial plane defines the *celestial equator*. The points of intersection with the polar axis are called the *celestial poles*. Using this form of representation, the movement of the Earth around the stationary sun may instead be seen as a movement of the Sun with the Earth taken as fixed. The sun then travels through a great circle of the celestial sphere, the *ecliptic*, which forms an angle of 23.45° with the celestial equator. The sun completes this circuit once a year while the celestial sphere rotates once a day around the Earth (regarded as fixed). In this way, the sun marks out a circle around the Earth. The diameter of the circle changes daily, reaching a maximum on the equinoxes and a minimum on the solstices. The rotation of the sun around the ecliptic is in the opposite direction to that of the celestial sphere around the Earth.

Now, landing on a particular location on the Earth's surface, where a PV system is going to be used, it is convenient to specify the position of the sun by means of two angles that refer to the horizontal plane and to the vertical. The vertical intersects the celestial sphere at points known as the zenith and the nadir. Figure 20.5 attempts to visualise these concepts. The *solar zenith angle*, θ_{zs} , is between the vertical and the incident solar beam; and the *solar azimuth*, ψ_s , is between the meridians of the location and the sun. The complement of the zenith angle is called the *solar altitude*, γ_s , and represents the angle between the horizon and the solar beam in a plane determined by the zenith and the sun. In the Northern (Southern) Hemisphere, the solar azimuth is referenced to south (north) and is defined as positive towards the west, that is, in the evening, and negative towards the east, that is, in the morning.

At any given moment, the angular coordinates of the sun with respect to a point of geographic latitude ϕ (north positive, south negative) are calculated from the equations:

$$\cos \theta_{zs} = \sin \delta \sin \phi + \cos \delta \cos \phi \cos \omega = \sin \gamma_s \quad (20.4)$$

and

$$\cos \psi_s = \frac{(\sin \gamma_s \sin \phi - \sin \delta)}{\cos \gamma_s \cos \phi} [\text{sign}(\phi)] \quad (20.5)$$

where ω is called the true solar time, or local apparent time, or solar hour, and is the difference between noon and the selected moment of the day in terms of a 360° rotation

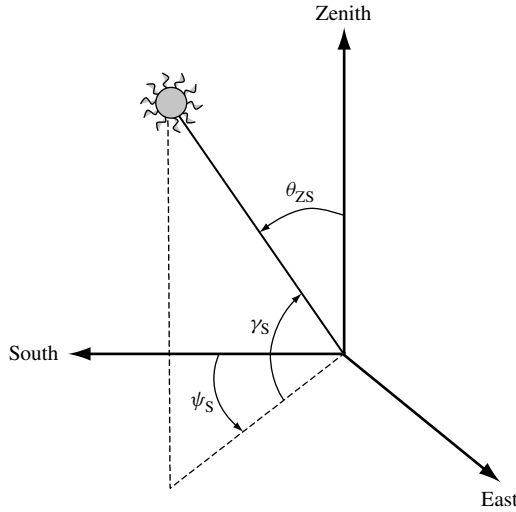


Figure 20.5 Position of the sun relative to a fixed point on the Earth

in 24 h. $\omega = 0$ at the midday of each day, and is counted as negative in the morning and positive in the afternoon. $[\text{sign}(\phi)]$ means “1” for northern latitudes and “-1” for southern latitudes. The true solar time ω is related to the local official time, TO , also called local standard time (the time shown by a clock) by the equation

$$\omega = 15 \times (TO - AO - 12) - (LL - LH) \quad (20.6)$$

where LL is the local longitude and LH is the reference longitude of the local time zone (positive towards the west and negative towards the east of the Greenwich Meridian). AO is the time by which clocks are set ahead of the local time zone. In the European Union, AO is usually one hour during winter and autumn, and two hours during spring and summer. In this equation ω , LL and LH are given in degrees, while TO and AO are given in hours.

Figure 20.6 presents the sun’s trajectory on the celestial sphere for (a) a winter and a summer day and (b) the corresponding plots of solar altitude versus azimuth. We will return to such plots later on.

Equation (20.4) may be used to find the *sunrise angle*, ω_s , since at sunrise $\gamma_s = 0$. Hence

$$\omega_s = -\arccos(-\tan \delta \tan \phi) \quad (20.7)$$

In accordance with the sign convention, ω_s is always negative. Obviously, the sunset angle is equal to $-\omega_s$ and the length of the day is equal to $2 \times \text{abs}(\omega_s)$. In the polar regions, during the winter the sun does not rise ($\tan \delta \tan \phi > 1$) and equation (20.7) has no real solution. However, for computing purposes, it is convenient to set $\omega_s = 0$. Similarly, during the summer, $\omega_s = -\pi$ is a practical solution for the continuous day. It is also interesting to note that just at noon, $\omega = 0$, and the solar altitude is equal to the latitude

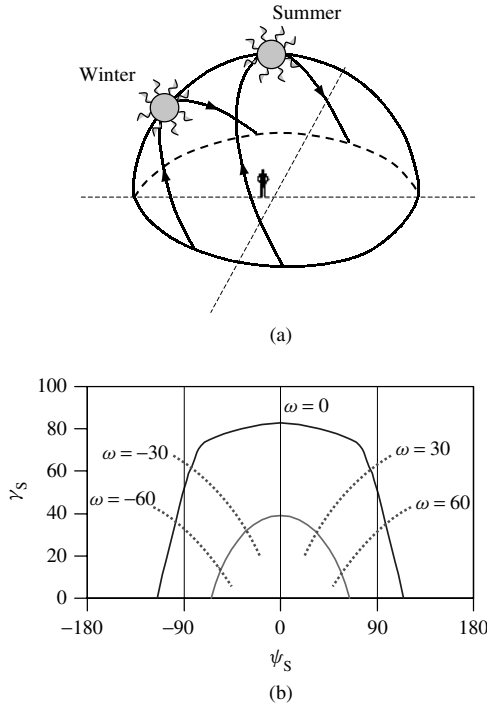


Figure 20.6 (a) Sun's trajectory corresponding to a winter and to a summer day represented over the celestial sphere. (b) The solar altitude γ_S is plotted against the solar azimuth ψ_S . The solar time ω is also shown

complement plus the declination

$$\omega = 0 \Rightarrow \gamma_S = \frac{\pi}{2} - \phi + \delta \quad (20.8)$$

It should be noted that equation (20.5) is indeterminate for $\gamma_S = \pi/2$ and for $\phi = \pi/2$. In the first case, the sun is just on the vertical, so that ψ_S is meaningless. In the second, the sun's position is given by $\gamma_S = \delta$ and $\psi_S = \omega$.

It should now be said that equations (20.1–20.3 and 20.6) derive from considering the angular velocity of the Earth through its elliptic orbit as constant, which is sufficiently accurate for most PV engineering applications. In particular, for all designs involving flat-plate PV modules, typical accuracy is about 1° . However, if desired, more accurate expressions are obtained when taking into account that the well-known Kepler's second law governs this angular velocity [2].

Another word of caution is necessary here. All the above-presented equations refer to a baseline year composed of 365 days, while the time length of the real year is 365 days, 5 h, 48 min and 45.9 s. As is well known, the difference is compensated by adding a day in the leap years. For most PV engineering applications, the same number corresponding to the precedent may be associated to this additional day, that is, $d_n = 59$ for both 28th and 29th of February. However, for some demanding applications, such as

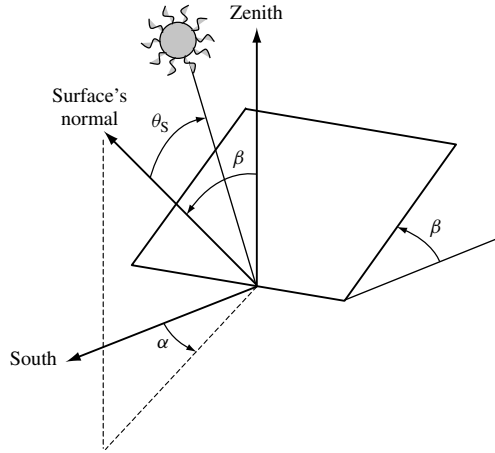


Figure 20.7 Receiver position (slope β and azimuth α) and sun's rays incidence angle θ_s

highly accurate trackers for concentrators, more precise equations may be necessary to calculate the relative Earth–Sun position. The interested reader is encouraged to consult Reference [3]. It describes an accurate algorithm and provides a software file for its implementation.

Equations (20.4) and (20.5) give the angles θ_{zs} and ψ_s relative to a horizontal surface. However, most practical applications require the position of the sun relative to an inclined plane to be determined. The position of a surface (Figure 20.7) may generally be described by its slope β (the angle formed with the horizontal) and the azimuth α of the normal to the surface. The angle of solar incidence between the sun's rays and the normal to the surface may be calculated from

$$\begin{aligned} \cos \theta_s = & \sin \delta \sin \phi \cos \beta - [\text{sign}(\phi)] \sin \delta \cos \phi \sin \beta \cos \alpha + \cos \delta \cos \phi \cos \beta \cos \omega \\ & + [\text{sign}(\phi)] \cos \delta \sin \phi \sin \beta \cos \alpha \cos \omega + \cos \delta \sin \alpha \sin \omega \sin \beta \end{aligned} \quad (20.9)$$

Although this expression appears quite complicated, it is very convenient to use in most instances. In the case of surfaces tilted towards the equator (facing south in the Northern Hemisphere, or facing north in the Southern Hemisphere), $\alpha = 0$, and it simplifies to

$$\cos \theta_s = [\text{sign}(\phi)] \sin \delta \sin(\text{abs}(\phi) - \beta) + \cos \delta \cos(\text{abs}(\phi) - \beta) \cos \omega \quad (20.10)$$

20.3 SOLAR RADIATION COMPONENTS

Figure 20.8 helps to illustrate the following brief explanation of the different components of solar radiation that reach a terrestrial flat-plate PV surface

To a good approximation, the sun acts as a perfect emitter of radiation (black body) at a temperature close to 5800 K. The resulting power incident on a unit area perpendicular to the beam outside the Earth's atmosphere, when it is 1 AU from the sun, is known as the *solar constant*

$$B_0 = 1367 \text{ W/m}^2 \quad (20.11)$$

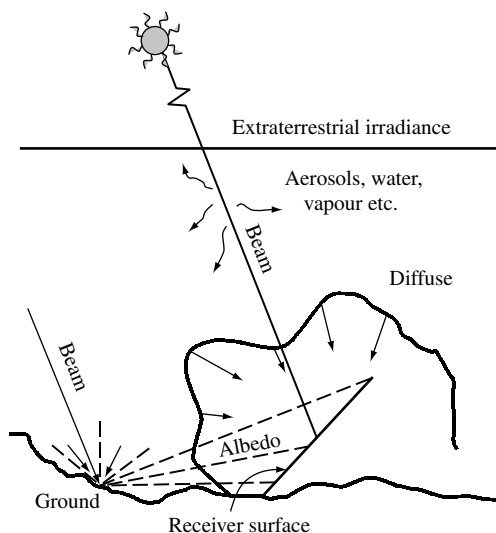


Figure 20.8 Different components of solar radiation

The radiation falling on a receiver situated beyond the Earth's atmosphere, that is, *extraterrestrial radiation*, consists almost exclusively of radiation travelling along a straight line from the sun. Since the intermediate space is almost devoid of material that might scatter or reflect the light, it appears virtually black, apart from the sun and faint points of light corresponding to the stars.

As the solar radiation passes through the Earth's atmosphere, it is modified by interaction with components present there. Some of these, such as clouds, reflect radiation. Others, for example, ozone, oxygen, carbon dioxide and water vapour, have significant absorption at several specific spectral bands. Water droplets and suspended dust also cause scattering. The result of all these processes is the decomposition of the solar radiation incident on a receiver at the Earth's surface into clearly differentiated components. *Direct or Beam radiation*, made up of beams of light that are not reflected or scattered, reaches the surface in a straight line from the sun. *Diffuse radiation*, coming from the whole sky apart from the sun's disc, is the radiation scattered towards the receiver. *Albedo radiation* is radiation reflected from the ground. The total radiation falling on a surface is the sum of these (direct + diffuse + albedo) and is termed *global radiation*.

It is intuitively obvious that the directional properties of the diffuse radiation depend to a large extent on the position, form and composition of the water vapor and dust responsible for scattering. The angular distribution of the diffuse radiation is therefore a complex function that varies with time. Diffuse radiation is essentially anisotropic. The amount of albedo radiation is greatly affected by the nature of the ground, and a wide range of features (snow, vegetation, water etc.) occur in practice.

In the following discussion, the word *radiation* will be used as a general term. To distinguish between power and energy, more specific terminology will be used. *Irradiance* means density of power falling on a surface, and is measured in W/m^2 (or similar); whereas *irradiation* is the density of the energy that falls on the surface over some

period of time, for example, hourly irradiation or daily irradiation, and is measured in Wh/m^2 . Furthermore, only the symbols B_0 , B , D , R and G will be used, respectively, for extraterrestrial, direct, diffuse, albedo and global irradiance, whereas a first subscript, h or d , will be used to indicate hourly or daily irradiation. A second subscript, m or y , will refer to monthly or yearly averaged values. Furthermore, the slope and orientation of the concerned surface are indicated among brackets. For example, $G_{\text{dm}}(20,40)$ refers to the monthly mean value of the daily global irradiation incident on a surface tilted $\beta = 20^\circ$ and oriented $\gamma = 40^\circ$ towards the west. For surfaces tilted towards the equator ($\gamma = 0$), only the slope will be indicated. For example, $B(60)$ refers to the value of the direct irradiance incident on a surface tilted $\beta = 60^\circ$ and oriented towards the south (in the Northern Hemisphere).

An important concept characterising the effect of atmosphere on clear days is the *air mass*, defined as the relative length of the direct-beam path through the atmosphere compared with a vertical path directly to sea level, which is designed as AM . For an ideal homogeneous atmosphere, simple geometrical considerations lead to

$$AM = \frac{1}{\cos \theta_{\text{ZS}}} \quad (20.12)$$

which is generally sufficient for most engineering applications. If desired, more accurate expressions, considering second-order effects (curvature of the Earth, atmospheric pressure etc.), are available [4].

At the standard atmosphere $AM\ 1$, after absorption has been accounted for, the normal irradiance is generally reduced from B_0 to $1000\ \text{W/m}^2$, which is just the value used for the standard test of PV devices (see Chapter 16). Obviously, that can be expressed as $1000 = 1367 \times 0.7^{AM}$. For general AM values, a reasonable fit to observed clear days data is given by [5].

$$G = B_0 \cdot \varepsilon_0 \times 0.7^{AM^{0.678}} \quad (20.13)$$

A particular example can help to clarify the use of these equations, by calculation of the sun co-ordinates and the global irradiance on a surface perpendicular to the sun, and also on a horizontal surface, over two geographic positions defined by $\phi = 30^\circ$ and $\phi = -30^\circ$, at 10:00 (solar time) on 14 April, being a clear day. The solution is as follows:

$$14\ \text{April} \Rightarrow d_n = 104; \varepsilon_0 = 0.993; \delta = 9.04^\circ$$

$$10:00\ \text{h} \Rightarrow \omega = -30^\circ$$

$$\phi = 30^\circ \Rightarrow \cos \theta_{\text{ZS}} = 0.819 \Rightarrow \theta_{\text{ZS}} = 35^\circ \Rightarrow \cos \psi_s = 0.508 \Rightarrow \psi_s = -59.44^\circ$$

$$\Rightarrow AM = 1.222 \Rightarrow G = 902.4\ \text{W/m}^2$$

$$\Rightarrow G(0) = G \cdot \cos \theta_{\text{ZS}} = 739\ \text{W/m}^2$$

$$\phi = -30^\circ \Rightarrow \cos \theta_{\text{ZS}} = 0.662 \Rightarrow \theta_{\text{ZS}} = 48.54^\circ \Rightarrow \cos \psi_s = 0.403 \Rightarrow \psi_s = -66.28^\circ$$

$$\Rightarrow AM = 1.510 \Rightarrow G = 846.9\ \text{W/m}^2$$

$$\Rightarrow G(0) = G \cdot \cos \theta_{\text{ZS}} = 561\ \text{W/m}^2$$

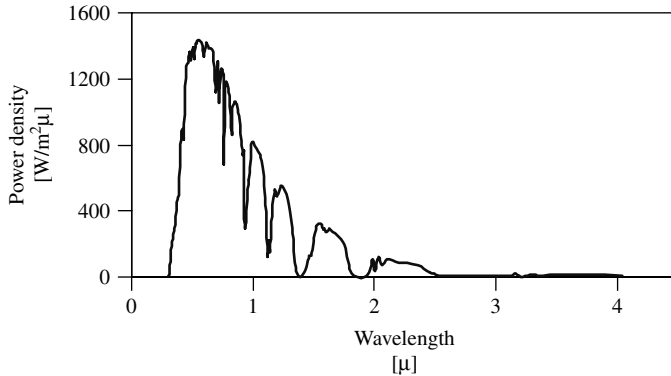


Figure 20.9 AM 1.5 solar spectrum, for an irradiance $G = 1000 \text{ W/m}^2$

When solar radiation enters the Earth's atmosphere, not only the irradiance but also the spectral content is affected. Figure 20.9 shows the AM 1.5 spectrum, which is considered for standard test of PV devices. Figure 16.1 shows other spectra for comparison. In general, increasing air mass displaces the solar spectrum towards the red. This is why the sky becomes so nice at nightfall.

Of course, PV devices are sensitive to the spectrum, as discussed in Chapters 3, 9, 12 and 16. However, this is of little importance from the PV engineering point of view, compared to changes in total radiation incident on the PV modules. Because of that, in what follows, we will omit the detailed treatment of the spectral composition of sunlight. Additional comments will be given later on in this chapter.

20.4 SOLAR RADIATION DATA AND UNCERTAINTY

The amount of global radiation that reaches the receiver is extremely variable. On the one hand, even the extraterrestrial radiation experiences regular daily and yearly variations due to the apparent motion of the sun. These variations are predictable and can be theoretically determined just by geometrical considerations. For example, the extraterrestrial irradiance over a horizontal surface is given by

$$B_0(0) = B_0 \varepsilon_0 \cos \theta_{zs} \quad (20.14)$$

which when integrated over the day, leads to [6]

$$B_{0d}(0) = \frac{T}{\pi} B_0 \varepsilon_0 \left[-\frac{\pi}{180} \omega_s \cdot \sin \delta \cdot \sin \phi - \cos \delta \cos \phi \sin \omega_s \right] \quad (20.15)$$

where T is the day length, that is, 24 h. The monthly average of this quantity, named $B_{0dm}(0)$, is of particular practical importance. Obviously

$$B_{0dm}(0) = \frac{1}{d_{n2} - d_{n1} + 1} \sum_{d_{n1}}^{d_{n2}} B_{0d}(0) \quad (20.16)$$

Table 20.1 Declination and extraterrestrial irradiation values for the characteristic day of each month

| Month | Date | d_n | δ [degrees] | $B_{0d}(0) = B_{0dm}(0)$, in [Wh/m ²] | | | |
|-----------|------|-------|-----------------------|--|-------------------|--------------------|--------------------|
| | | | | $\phi = 30^\circ$ | $\phi = 60^\circ$ | $\phi = -30^\circ$ | $\phi = -60^\circ$ |
| January | 17 | 17 | -20.92 | 5 907 | 949 | 11 949 | 11 413 |
| February | 14 | 45 | -13.62 | 7 108 | 2 235 | 11 062 | 9 083 |
| March | 15 | 74 | -2.82 | 8 717 | 4 579 | 9 531 | 5 990 |
| April | 15 | 105 | +9.41 | 10 225 | 7 630 | 7 562 | 3 018 |
| May | 15 | 135 | +18.79 | 11 113 | 10 171 | 5 948 | 1 225 |
| June | 10 | 161 | +23.01 | 11 420 | 11 371 | 5 204 | 605 |
| July | 18 | 199 | +21.00 | 11 224 | 10 741 | 5 530 | 878 |
| August | 18 | 230 | +12.78 | 10 469 | 8 440 | 6 921 | 2 294 |
| September | 18 | 261 | +1.01 | 9 121 | 5 434 | 8 835 | 4 937 |
| October | 19 | 292 | -11.05 | 7 436 | 2 726 | 10 612 | 8 226 |
| November | 18 | 322 | -19.82 | 6 056 | 1 114 | 11 754 | 10 983 |
| December | 13 | 347 | -23.24 | 5 498 | 613 | 12 174 | 12 177 |

where d_{n1} and d_{n2} are the day numbers of the first and last day of the month, respectively. It is useful to know that, for a given month, there is a day for which $B_{0d}(0) = B_{0dm}(0)$. It can be demonstrated that this day is the one whose declination equals the mean declination for the month. Table 20.1 shows the day number of this day and the corresponding value of $B_{0dm}(0)$ for each month of the year at several latitudes.

We have also shown that the effect of clear cloudless skies can be predictably accounted for by a single geometrical parameter, namely, the Air Mass (equation 20.12). On the other hand, there are random variations caused by climatic conditions: cloud cover, dust storms and so on so that the PV systems design should rely on the input of measured data close to the site of the installations and averaged over a long time. This is routinely done by the National Meteorological Services (or similar services), which use a variety of instruments and procedures, from direct sunlight measurements (pyranometers, pyrhemometers etc.) to correlations with other meteorological variables (hours of sunshine, cloudiness, tone of satellite photographs etc). Then, they are treated to derive some representative parameters, which are made publicly available by different ways: World radiation databases [7, 8], Regional [9], National [10–12] and local [13] Radiation Atlas, web sites [14, 15] and so on. The 12 monthly mean values of global horizontal daily irradiation, $G_{dm}(0)$, today represent the most widely available information concerning the solar radiation resource, and that is likely to remain in the years to come. It is important to note that solar radiation unavoidably represents a large source of uncertainty for PV systems designers, as revealed by the significant disparity between different information sources. As a representative example, we will consider the case of Madrid.

The Spanish National Meteorological Institute has been recording daily values of hours of sunshine from 1951 to 1980, and hourly global horizontal irradiation data since 1973. This means that the Madrid solar radiation data bank is today composed of more than 50 years of daily indirect observations and more than 25 years of hourly direct ones. Such comprehensive data may appear very gratifying. However, an in-depth examination of the data bank reveals several difficulties: significant data gaps (the most important extends from June 1988 to July 1989); changes of the sensor's calibration constant (in

1977, the IPS-1956 reference was substituted by the WRP); and inconsistencies between global, direct and diffuse irradiation values due to mistakes in graphic record evaluation. All these difficulties must be overcome when computing statistical representative values. Different researchers use different procedures (for example, when considering a set of data of doubtful quality, one can opt to use it directly, or to estimate a best value, or simply to neglect it), arriving at different results. Furthermore, different researchers use different data recording periods for computing representative values (because solar radiation data are being constantly and routinely recorded, this is usually the case). The astonishing result is that a large disparity in representative values is found for the same location, when different publications are consulted. Table 20.2 presents the $G_{dm}(0)$ values for Madrid according to different publications. Large disparities are evident and deserve further comment, because they translate into serious practical consequences. For example, for sizing the PV generator of a stand-alone PV system, it is customary to select the so-called worst month, that is, the month with the lowest value of $G_{dm}(0)$. It is clear that irrespective of the selected sizing methodology, the choice of the particular solar radiation database for Madrid involves PV array size differences up to 12% $[(1.58-1.77)/1.58]$, far beyond the claimed accuracy of most presently available PV sizing methods.

It is important to note that, despite the above-mentioned difficulties, concerning rough solar radiation data, the uncertainty does not derive primarily from a lack of perfect precision in the measuring instruments, but rather from the random nature of the solar radiation, that is, from the overall statistical fluctuations in the collection of finite number of counts over finite intervals of time. This leads us to the question of the real representativeness of the data, or, in more strict terms, to the “confidence” we have that average values, based on past observations of solar radiation, are a correct prediction of the future solar radiation. A close look at the rough recorded data can help to elucidate this question. Figure 20.10 shows the January $G_{dm}(0)$ values corresponding to the years 1979 to 1986, for which very accurate data – let us say, 3% of accuracy – are available, according to Reference [16]. The average value is $\overline{G_{dm}(0)} = 1.99 \text{ kWh/m}^2$. We could then give this value as our estimate for the future. However, if someone now asked the question, “What is the probability that the future $G_{dm}(0)$ will be exactly 1.99 kWh/m^2 ?”, we would have to answer – somewhat uncomfortably – that the probability is no doubt close to zero. However, we would have to hasten to add that if we relax the prediction rigour, just saying that the future $G_{dm}(0)$ values will be within the range of 1.55 to 2.58 kWh/m^2 , as in Figure 20.10, then the probability is high. Note that this range represents $\pm 26\%$ of the

Table 20.2 Values of the mean global daily irradiances $G_{dm}(0)$, in kWh/m^2 , in Madrid according to different publications

| Ref | Jan | Feb | Mar | Apr | May | June | July | Aug | Sep | Oct | Nov | Dec | Year |
|------|------|------|------|------|------|------|------|------|------|------|------|------|------|
| [7] | 1.86 | 2.94 | 3.78 | 5.22 | 5.80 | 6.53 | 7.22 | 6.42 | 4.69 | 3.17 | 2.08 | 1.64 | 4.29 |
| [16] | 1.99 | 2.64 | 4.32 | 5.32 | 6.28 | 7.29 | 7.47 | 6.62 | 5.11 | 3.40 | 2.16 | 1.72 | 4.53 |
| [94] | 2.29 | 2.81 | 4.48 | 5.25 | 6.60 | 7.24 | 7.55 | 6.33 | 5.22 | 3.62 | 2.10 | 1.64 | 4.60 |
| [10] | 2.0 | 2.8 | 4.4 | 5.4 | 6.6 | 7.4 | 7.8 | 7.0 | 5.4 | 3.6 | 2.6 | 1.8 | 4.7 |
| [9] | 1.73 | 2.63 | 4.15 | 5.45 | 6.17 | 6.69 | 7.22 | 6.49 | 4.80 | 3.16 | 1.99 | 1.77 | 4.36 |
| [95] | 2.0 | 2.91 | 3.92 | 5.34 | 6.31 | 6.95 | 7.09 | 6.31 | 4.73 | 3.30 | 2.18 | 1.74 | 4.41 |
| [96] | 2.13 | 2.75 | 4.55 | 5.10 | 6.58 | 7.43 | 7.42 | 6.48 | 5.00 | 3.39 | 2.13 | 1.58 | 4.55 |
| [14] | 1.94 | 2.76 | 4.05 | 4.84 | 5.79 | 6.47 | 7.05 | 6.24 | 4.87 | 3.07 | 1.98 | 1.61 | 4.23 |

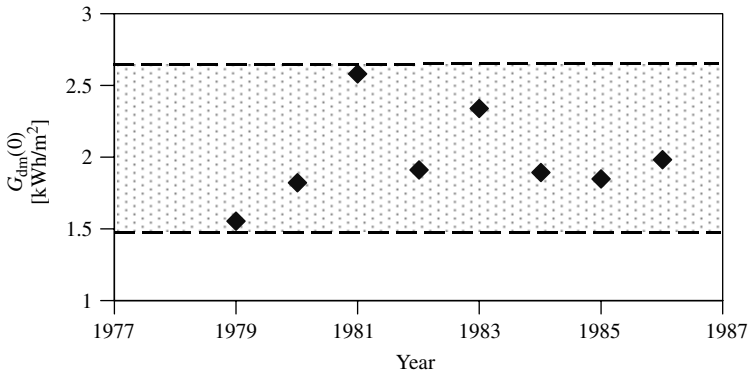


Figure 20.10 January means of the global horizontal irradiation $G_{dm}(0)$ in Madrid, for the years 1979 to 1986, in kWh/m²

average value, much larger than the accuracy of the original data! Then, our questioner's retort would probably be, "How 'high' is the probability and how 'large' is the range?"

Basic statistical theory [17] gives proper answers to this question. For example, if we desire a 99% probability (the *confidence coefficient*) we must keep a $\pm 3\sigma$ range (the *confidence interval*) around the average value, in which σ is the *standard deviation* of the past observed values. In our example, $\sigma = 0.31$ kWh/m², so that $\pm 3\sigma$ represents $\pm 47\%$ of the average value. Still larger than the previously considered range, noted by the band of Figure 20.10! In order to keep on intervals of practical use, a $\pm 2\sigma$ interval is often employed. The corresponding confidence interval is 95%. In our example, $\pm 2\sigma$ represents $\pm 31\%$. Using the 2σ confidence level, the correct way to state the daily global irradiation prediction for the next January would be to say

$$1.37 \text{ kWh/m}^2 \leq G_{dm}(0) \leq 2.61 \text{ kWh/m}^2$$

or

$$G_{dm}(0) = 1.99 \text{ kWh/m}^2 \pm 31\%$$

Probably, surprised by such large uncertainty ($\pm 31\%$ seems badly matched and inconsistent with the "high accuracy" image generally associated with modern computational technology), our questioner would retort, "How can this uncertainty be reduced?" In fact, the only way is by enlarging the number of years of the future for which the prediction applies. That is, to give an estimate not for the next January, but for the average value of the following Januarys. Then, it can be shown that the confidence interval becomes reduced by a factor of $1/\sqrt{N}$, N being the number of future years for which the prediction is extended. Coming back to our example, and considering a future length of 10 years, the correct prediction would be

$$1.79 \text{ kWh/m}^2 \leq G_{dm}(0) \leq 2.19 \text{ kWh/m}^2$$

or

$$G_{dm}(0) = 1.99 \text{ kWh/m}^2 \pm 10\%$$

And still, we are disregarding the instrumental errors – at least $\pm 3\%$ in the best series of solar radiation data – and the causes of variability that can be hidden on a series of only 20 years of data. For example, the ones associated with the Global Climatic Change due to the global emissions of CO_2 . As a matter of fact, it should be noted that some of the $G_{\text{dm}}(0)$ values listed in Table 20.2 for January fall outside this range.

Table 20.3 shows the uncertainty parameters for each month and for the entire year for Madrid, based on data of Reference [16]. It is worth observing that monthly uncertainty is greater in winter than in summer (this is because summer solar radiation is dominated by clear days, essentially governed by the predictable extraterrestrial radiation, while winter solar radiation is strongly influenced by cloudy days, which are governed by random atmospheric phenomena). Besides, uncertainty becomes substantially lower when the whole year is considered (this is because yearly data result from greater aggregates than monthly data, and it is a basic law that the greater the aggregation, the lower the dispersion of the corresponding results). Later on, we will analyse the implications for different PV applications. It should be said that the IES experience in designing PV systems for different locations around the world has led us to believe that the above-described, concerning solar radiation data sources for Madrid, far from being a particular case, is rather representative of a general situation. For example, the December mean daily global horizontal irradiation in New York is $G_{\text{dm}}(0) = 1.36 \text{ kWh/m}^2$ according to Reference [7], 1.47 kWh/m^2 according to Reference [14], and 1.6 kWh/m^2 according to Reference [15]. The interested reader is encouraged to also consult Reference [18].

It is rather obvious that, whatever the detailed methodology, the PV-system design is essentially a prediction exercise extended over the expected system lifetime. From the previous considerations, it follows that such a prediction exercise is unavoidably associated with a rather large degree of uncertainty. Irrespective of whether good historical data are available and whether more complex models are used, any attempt to overcome such uncertainty is simply wrong. We should insist on that because, unfortunately, many authors often forget it when proposing PV-system design tools. This false sense of predictability and regularity in the solar radiation is, to a certain extent, being boosted by the proliferation of software-based tools, that are able to perform extremely detailed simulations with large sequences of solar radiation data. The great “accuracy” of their calculations tends to confer an impressive “scientific” appearance to these tools, and foster the tendency to believe that their results are superior to others. However, the truth is that such great accuracy is statistically meaningless, and that, much more simple design methodologies can yield results of similar confidence. We should keep this idea in mind all through this chapter.

Table 20.3 Solar radiation parameters for Madrid. Mean G_{dm} and standard deviation values σ are given in kWh/m^2 , while $2\sigma/G_{\text{dm}}$ is given in %

| | Jan | Feb | Mar | Apr | May | June | July | Aug | Sep | Oct | Nov | Dec | Mean |
|-------------------------|------|------|------|------|------|------|------|------|------|------|------|------|------|
| G_{dm} | 1.99 | 2.64 | 4.32 | 5.32 | 6.28 | 7.29 | 7.47 | 6.62 | 5.11 | 3.4 | 2.16 | 1.72 | 4.53 |
| σ | 0.31 | 0.31 | 0.36 | 0.39 | 0.64 | 0.34 | 0.31 | 0.18 | 0.36 | 0.39 | 0.36 | 0.17 | 0.08 |
| $2\sigma/G_{\text{dm}}$ | 31 | 23 | 17 | 15 | 20 | 9 | 8 | 8 | 14 | 23 | 34 | 20 | 4 |

20.4.1 Clearness Index

The relation between the solar radiation at the Earth's surface and the Extraterrestrial radiation gives a measure of the atmospheric transparency. This way, a *clearness index*, K_{Tm} , is calculated for each month:

$$K_{Tm} = \frac{G_{dm}(0)}{B_{0dm}(0)} \quad (20.17)$$

Note that the clearness index is physically related not only to the radiation path through the atmosphere, that is, with the AM value, but also with the composition and the cloud content of the atmosphere. Liu and Jordan [19] have demonstrated that, irrespective of latitude, the fractional time during which daily global radiation is equal to or less than a certain value is directly dependent on this parameter. Because of that, K_{Tdm} can properly characterise the solar climate of a particular location. This provides the basis for estimating solar radiation on inclined surfaces.

20.5 RADIATION ON INCLINED SURFACES

To eliminate the effects of varying local features, such as obstructions that cast shadows and the specific ground covering, solar radiation is routinely measured on horizontal surfaces free of obstacles. Consequently, solar radiation data are most often given in the form of global radiation on a horizontal surface. Since PV modules are usually positioned at an angle to the horizontal plane, the radiation input to the system must be calculated from the data.

The assessment of radiation arriving on an inclined surface, using as input global horizontal data, raises two main problems: to separate the global horizontal radiation into their direct and diffuse components; and, from them, to estimate the radiation components falling on an inclined surface. In general, these problems may be posed for different time scales, for example, daily irradiation, hourly irradiation and so on. Individual or time-averaged values may be sought. Here, we will first focus on the monthly average daily irradiation values. This is not only convenient for presentation purposes, but also coherent with solar radiation data availability, and particularly suited to afford most PV engineering practical problems. Additional comments for other cases will also be given afterwards.

20.5.1 Estimation of the Direct and Diffuse Components of Horizontal Radiation, Given the Global Radiation

The underlying concept is the one originally proposed by Liu and Jordan [19]. It consists of establishing empirical correlation between the *diffuse fraction of horizontal radiation*, $F_{Dm} = D_{dm}(0)/G_{dm}(0)$, (diffuse radiation/global radiation) and the *clearness index* (global radiation/extraterrestrial radiation) defined in equation (20.17). Note that the clearer the atmosphere, the higher the radiation and the lower the diffuse content. Hence, F_{Dm} and K_{Tdm} are expected to be negatively correlated. Actual analytical expressions are established from the comparison of simultaneous measurements of global and diffuse radiation

performed in certain places. Liu and Jordan were, in fact, very clever in selecting the clearness index (which they called the cloudiness index) to characterise the solar climate at a particular location, because the division by the extraterrestrial radiation eliminates the radiation variations due to the apparent motion of the sun. This way, the correlation between F_{Dm} and K_{Tm} becomes independent of latitude effects, and, in principle, tends to be of universal validity.

Various empirical formulae are available. Using data from ten locations situated between 40°N and 40°S , Page [20] recommended a liner equation that has been frequently identified as the one giving the best results.

$$F_{Dm} = 1 - 1.13K_{Tm} \quad (20.18)$$

Figure 20.11 plots equation (20.18) and a set of experimental points, obtained in Madrid, from 1977 to 1988.

Example: Determination of direct and diffuse components of the global radiation for the month of June in a location having a latitude $\phi = 30^\circ$ and a mean global horizontal daily irradiation $G_{dm}(0) = 6100 \text{ Wh/m}^2$. The solution is

$\phi = 30$ and June $\Rightarrow B_{0dm}(0) = 11\,420 \text{ Wh/m}^2$ (See Table 20.1)

$$G_{dm}(0) = 6100 \text{ Wh/m}^2 \Rightarrow K_{Tm} = 0.534 \Rightarrow F_{Dm} = 0.396 \Rightarrow D_{dm}(0) = 2418 \text{ Wh/m}^2$$

$$\Rightarrow B_{dm}(0) = 3682 \text{ Wh/m}^2$$

Empirical correlations between the diffuse fraction of the horizontal irradiation and the clearness index can also be derived for an individual day (April 14 is, for example, an individual day, while generic April is a monthly mean day). They should be described here because they have been the object of extensive research in the general solar radiation community and, as a result they have received large attention in the available literature, and they are often employed in today's available PV engineering software tools. However, it should be advised that their advantage for PV design purposes is far from clear. As a matter of fact, the electrical behaviour of PV generators is mainly governed by the linear

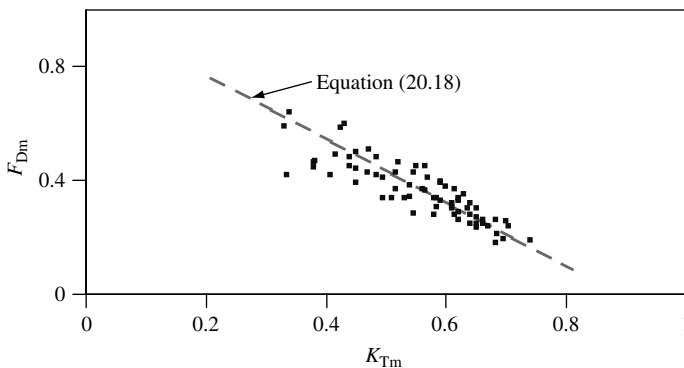


Figure 20.11 The diffuse fraction of the mean daily global irradiation F_{Dm} is plotted against the clearness index K_{Tm} . The cluster of points refers to measured values in Madrid from 1977 to 1988

dependence incident irradiance. It follows that the mean power they deliver during a period of time tends to be equal to the delivered power when they are illuminated with the mean irradiance during such time. Second-order effects, associated to ambient temperature or operation voltage fluctuations, do not significantly alter this idea, provided that they are adequately considered, as discussed afterwards. Because of that, rather few benefits, in terms of long-term performance predictions, should be expected from analysing all the days of a month instead of only the mean day of such a month. The reason for the popularity of individual day analysis in recently available software tools, lies more with fashion and prestige than with increasing energy yield prediction certainty.

Figure 20.12 shows the experimental values of $F_{Dd} = D_d(0)/G_d(0)$ versus $K_{Td} = G_d(0)/B_{0d}(0)$, obtained in Madrid, from 1977 to 1988. Each point derives from the simultaneous measurement of the diffuse and the global horizontal irradiation along a particular day. Note that the general trend is consistent with the principle that the clearer the atmosphere, the lower the diffuse content. A third-order or fourth-order polynomial in K_{Td} is generally used to model the diffuse fraction F_{Dd} . A correlation between F_{Dd} and K_{Td} was first developed by Liu and Jordan [19]. However, it was derived from diffuse radiation data that were not compensated for by shadow-band effects (the shadow band is a device added to a pyranometer, to exclude the direct radiation from the sun. Hence, it allows for the measurement of diffuse radiation. However, the shadow-band screens the sensor not only from the sun but also from a portion of the diffuse radiation coming in from the sky, so that, a correction must be made to the measurement). Not surprisingly, later revisions by other authors concluded that the Liu and Jordan correlation underestimates diffuse radiation.

The most frequently referred correlation for daily values is that put forward by Collares Pereira and Rabl [21], using data from five stations located in the United States. It is expressed as

$$F_{Dd} = 0.99 \text{ for } K_{Td} \leq 0.17$$

$$F_{Dd} = 1.188 - 2.272K_{Td} + 9.473K_{Td}^2 - 21.856K_{Td}^3 + 14.648K_{Td}^4 \quad (20.19)$$

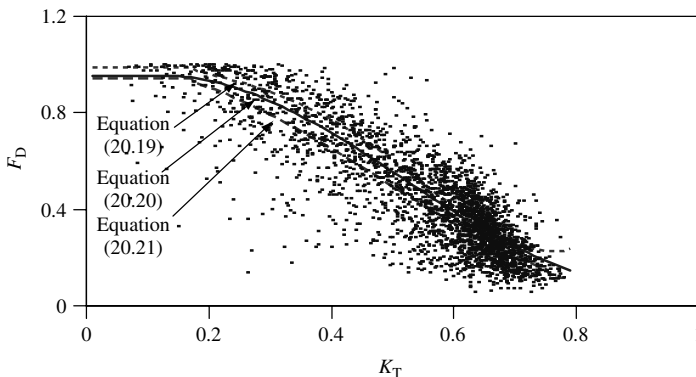


Figure 20.12 The diffuse fraction of the individual daily global irradiation F_{Dd} is plotted against the clearness index K_{Td} . The cluster of points refers to measured values in Madrid from 1977 to 1988

Despite independence of latitude, other second-order factors can affect the observed correlations, leading to a certain site dependence. For example, at very high latitudes, perennial snow cover could significantly increase diffuse radiation caused by multiple reflections between the ground and cloud cover. Also, atmospheric humidity tends to increase scattering, in relative terms. Hence, for a given clearness index, locations with low humidity will tend to have the lowest diffuse radiation content. Because of that, and because radiation data are still being accumulated and revised, new correlations are continuously enlarging the available literature. A recent study [22], devoted to the development of solar radiation models for the Mediterranean area, has found about 250 different correlations in the literature. The same study, extended to more than 150 000 pairs of data from eleven different stations of the European network, has proposed the following expression

$$\begin{aligned}
 F_{Dd} &= 0.952 \text{ for } K_{Td} \leq 0.13 \\
 F_{Dd} &= 0.868 + 1.335K_{Td} - 5.782K_{Td}^2 + 3.721K_{Td}^3 \\
 &\quad \text{for } 0.13 < K_{Td} \leq 0.8 \\
 F_{Dd} &= 0.141 \text{ for } K_{Td} > 0.8
 \end{aligned} \tag{20.20}$$

Local correlations that are derived from the data of only one site can also be found. As an example, Macagnan [16] proposed the following for Madrid

$$\begin{aligned}
 F_{Dd} &= 0.942 \text{ for } K_{Td} \leq 0.18 \\
 F_{Dd} &= 0.974 + 0.326K_{Td} - 3.896K_{Td}^2 + 2.661K_{Td}^3 \\
 &\quad \text{for } 0.18 < K_{Td} \leq 0.79 \\
 F_{Dd} &= 0.115 \text{ for } K_{Td} > 0.79
 \end{aligned} \tag{20.21}$$

Such diversity of correlations can again perplex our hypothetical questioner, who would ask, “What correlation should I use?” Hence, it is worth to study further the implications of using one or the other.

On the one hand, it should be remembered that the uncertainty associated with the variability of observed individual data, as described in the previous section for global radiation, also applies here. The cluster of (F_{Dd}, K_{Td}) points in Figure 20.12 reveals that, for a given K_{Td} , very different F_{Dd} values can be found in reality. For example, the observed range for $K_{Td} = 0.5$ is $0.1 \leq F_{Dd} \leq 0.7$, that is $\pm 75\%$ around the mean value. In more strict terms, a measure of the dispersion of expected observations around the prediction derived from a particular correlation, is given by the so-called Root Mean Square Error, or Standard Error of Estimate, s_e . As with the standard deviation, $\pm 2s_e$ is the interval, around the predicted value, for 95% confidence. In general, s_e are larger than 25%, which means that, regardless of the selected correlation, we would nearly always expect real values of diffuse irradiation for individual days falling between $\pm 50\%$ of the predictions. It is also interesting to observe that the dispersion associated with individual days (Figure 20.12) is significantly larger than the dispersion associated with monthly means (Figure 20.11).

On the other hand, when long-term performance predictions are concerned – which is the standard case on PV design – the implications of using different correlations are in

fact very modest. As a representative exercise, we have calculated the daily irradiation incident on a surface tilted to the latitude in Djelfa-Algeria ($\phi = 34.6^\circ$), for a winter day ($d_n = 17$) and for a summer day ($d_n = 161$), using the different correlations defined by equations (20.19–20.21). Djelfa and Madrid are relatively similar on geographical altitude and solar climate. Hence, it is reasonable to assume that the same local correlation could be applied to both places. $G_d(0) = 2778$ and 6972 Wh/m^2 for the winter and for the summer day, respectively. This radiation data has been obtained from Reference [7], by assuming that the value of the global irradiation during these days coincides with the corresponding monthly averages. Details of the calculating procedure will be given in the next section, but they are not relevant for the present discussion. The results are as follows:

$$d_n = 17 \Rightarrow B_{0d}(0) = 5177 \text{ Wh/m}^2$$

$$G_d(0) = 2778 \text{ Wh/m}^2 \Rightarrow K_{Td} = 0.537$$

| Eq. | F_{Dd} | $D_d(0)$ in [Wh/m ²] | $G_d(\phi)$ in [Wh/m ²] |
|-------|----------|-------------------------------------|--|
| 20.19 | 0.5301 | 1472 | 3946 |
| 20.20 | 0.5067 | 1408 | 4008 |
| 20.21 | 0.4351 | 1209 | 4185 |

$$d_n = 161 \Rightarrow B_{0d}(0) = 11\,525 \text{ Wh/m}^2$$

$$G_d(0) = 6972 \text{ Wh/m}^2 \Rightarrow K_{Td} = 0.605$$

| Eq. | F_{Dd} | $D_d(0)$ in [Wh/m ²] | $G_d(\phi)$ in [Wh/m ²] |
|-------|----------|-------------------------------------|--|
| 20.19 | 0.4034 | 2813 | 5988 |
| 20.20 | 0.4031 | 2811 | 5988 |
| 20.21 | 0.3345 | 2332 | 5940 |

Significant differences are observed in the estimation of the diffuse component of the horizontal irradiation. However, the noticeable key point is that these differences are significantly lessened in the estimation of the global irradiation. For example, for the winter day, differences on the diffuse component reach 22% while differences on the global radiation are lower than 6%.

Now, it is worth noting that, to a certain extent, we can cite a physical reason for the differences, considering the primary role of scattering in the diffusion of solar radiation. Equation (20.19) was derived from northern latitudes, with higher air masses than the Mediterranean region (higher air mass means higher scattering and, consequently, higher diffuse radiation content), and Madrid is a relatively high altitude site (670 m over the sea level) and its climate is essentially dry (both, higher altitude and lesser humidity

means lesser scattering). Note that the correlative order of the results agrees with this physical explanation.

To summarize, an adequate answer to our hypothetical questioner is as follows:

1. Most PV engineering problems are properly solved using a monthly mean analysis. Then, equation (20.18) is the recommended choice.
2. If you require a day-to-day analysis, the choice of a particular diffuse-to-global correlation is not really critical. You can simply adhere to the widely extended practise of trusting on the “universal” character of equation (20.19). But, if you are interested in a specific site, you can perform slightly better by choosing a more site-specific correlation, providing it is derived from solar radiation measurements in a place having a similar climate to the concerned site.
3. Whichever possibility you choose, you must take a very important precaution. If your results are going to be compared with the results of another calculation (for example, comparing different PV module orientations for the same application), then be sure that they both use the same assumptions, correlations, model and data. Otherwise, the differences in the results would be completely meaningless. Although this caveat should be obvious, it still should be mentioned, because the literature contains several examples of different results derived from different correlations that were proposed as the basis of optimisation design exercises [23].

Finally, it should be mentioned that not only daily but also hourly based correlations have been proposed. These are correlations between the diffuse fraction of the hourly horizontal global irradiation, $F_{Dh} = D_h(0)/G_h(0)$, and the hourly clearness index, $K_{Th} = G_h(0)/B_{0h}(0)$. However, none of the hourly based correlations proposed so far is really satisfactory [6, 22], so that the associated complexity is not justified. Hence, they will be not considered here.

20.5.2 Estimation of the Hourly Irradiation from the Daily Irradiation

In some cases, the treatment of solar radiation is more easily understood at the instant time scale, that is, at the radiance level. Because irradiation over an hour (in Wh/m^2) is numerically equal to the mean irradiance during this hour (in W/m^2), irradiance values can be, to a certain extent, assimilated to hourly irradiation values. However, since the availability of hourly irradiation data is limited, the problem is how to estimate the hourly irradiation, given the daily irradiation.

To introduce the solution to this problem, it is highly instructive to observe that, in terms of extraterrestrial horizontal radiation, the ratio between irradiance, $B_0(0)$, and daily irradiation, $B_{0d}(0)$, can be theoretically determined from equations (20.4), (20.14) and (20.15).

$$\frac{B_0(0)}{B_{0d}(0)} = \frac{\pi}{T} \times \frac{\cos \omega - \cos \omega_S}{\left(\frac{\pi}{180} \omega_S \cos \omega_S - \sin \omega_S \right)} \quad (20.22)$$

where the sunrise angle, ω_S , is expressed in degrees and T , the day length, is usually expressed in hours.

From the examination of data from several stations, it has been repeatedly noted [19, 24] that, considering long-term averages of terrestrial radiation, the correspondence between the measured ratio of diffuse irradiance to diffuse daily irradiation, $r_D = D(0)/D_d(0)$, and this theoretical expression for extraterrestrial radiation (equation 20.22) is quite good, while the correspondence between the measured ratio of global irradiance to global daily irradiation, $r_G = G(0)/G_d(0)$, and this expression, although not perfect, is quite close, so that a slight modification is required to fit the observed data. The following expressions apply [21]:

$$r_D = \frac{D(0)}{D_d(0)} = \frac{B_0(0)}{B_{0d}(0)} \quad (20.23)$$

and

$$r_G = \frac{G(0)}{G_d(0)} = \frac{B_0(0)}{B_{0d}(0)}(a + b \cos \omega) \quad (20.24)$$

where a and b are obtained from the following empirical formulae:

$$a = 0.409 - 0.5016 \times \sin(\omega_S + 60) \quad (20.25)$$

and

$$b = 0.6609 + 0.4767 \times \sin(\omega_S + 60) \quad (20.26)$$

Note that r_D and r_G have units of T^{-1} , and that they can be extended to calculate irradiances during short periods centred on the considered instant, ω . For example, if we wish to evaluate the irradiation over one hour between 10:00 and 11:00 (in solar time), we set $\omega = -22.5^\circ$ (the centre time of the considered period is 10:30, i.e. one hour and half, or 22.5° , before noon) and $T = 24$ h. If we wish to evaluate the irradiation over one minute, we just have to express T in minutes, that is, we set it to 1440, the number of minutes in a day.

An example can help in the use of these equations: the calculation of the irradiance components at several moments along the 15 April in Portoalegre–Brasil ($\phi = -30^\circ$), knowing the global daily irradiation, $G_d(0) = 3861 \text{ Wh/m}^2$. The results are as follows:

$$d_n = 105 \Rightarrow B_{0d}(0) = 7562 \text{ Wh/m}^2 \Rightarrow K_{Td} = 0.5106 \Rightarrow F_{Dd} = 0.423$$

$$\Rightarrow D_d(0) = 1633 \text{ Wh/m}^2$$

$$\omega_S = -84.51^\circ$$

$$\frac{\pi}{180} \omega_S \cos \omega_S - \sin \omega_S = 0.8542$$

$$a = 0.6172$$

$$b = 0.4672$$

$$r_D = 0.0922(\cos \omega + 0.0967) \text{ h}^{-1}$$

$$r_G = r_D(a + b \cos \omega)$$

| ω° | r_D [h ⁻¹] | r_G [h ⁻¹] | $D(0)$ in [Wm ⁻²] | $G(0)$ in [Wm ⁻²] | $B(0)$ in [Wm ⁻²] |
|----------------|-----------------------------|-----------------------------|----------------------------------|----------------------------------|----------------------------------|
| ω_s | 0 | 0 | 0 | 0 | 0 |
| ± 60 | 0.0618 | 0.0529 | 100.94 | 204.25 | 103.31 |
| ± 30 | 0.1177 | 0.1211 | 192.24 | 467.58 | 275.34 |
| 0 | 0.1382 | 0.1508 | 225.73 | 582.24 | 356.51 |

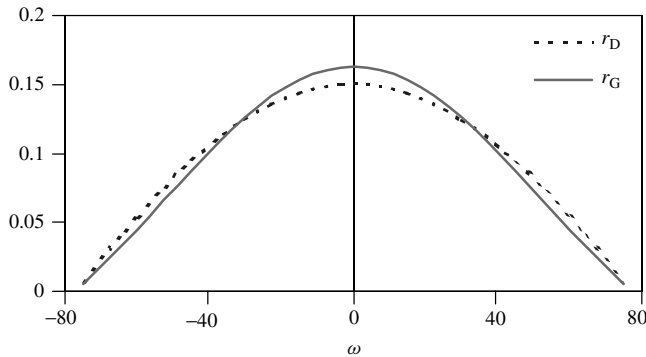


Figure 20.13 Plots of irradiance to daily irradiation ratios, for both diffuse and global radiation, r_D and r_G , along the day at a latitude $\phi = -30^\circ$ for 15 April

Figure 20.13 plots r_D and r_G versus the solar time, along the day. It is interesting to observe that r_G is slightly more sharp-pointed than r_D . This is because, due to air mass variations, beam transmittance is higher at noon than at any other moment of the day. Obviously, integrating the areas below both, r_D and r_G must be equal to one. As already mentioned, for this calculation it can be assumed that the irradiance over one hour (in Wh/m²) is numerically equal to the mean irradiance during this hour and also equal to the irradiance at the instant half way through the hour. For example, the global irradiance at noon, $G(0) = 580.4 \text{ W/m}^2$ can be identified with the hourly irradiation from 11:30 to 12:30, $G_h(0) = 580.4 \text{ Wh/m}^2$. This assumption does not introduce significant errors and it greatly simplifies the calculations by eliminating the need to evaluate integrals with respect to time, which, otherwise, can be quite tedious.

From these equations, it can be deduced that, on any day of the year and anywhere in the world, 90% of the total global horizontal irradiation is received during a period centred around midday and of length equal to two-thirds the total sunlight day length. Consequently, a stationary receiver tilted to the equator ($\alpha = 0$) captures all the useful energy in this period. The same need not be true, however, of receivers that track the sun.

20.5.3 Estimation of the Radiation on Surfaces on Arbitrary Orientation, Given the Components Falling on a Horizontal Surface

The most obvious procedure for calculating the global irradiance on an inclined surface, $G(\beta, \alpha)$, is to obtain separately the direct, diffuse and albedo components, $B(\beta, \alpha)$,

$D(\beta, \alpha)$ and $R(\beta, \alpha)$, respectively. Once these are known

$$G(\beta, \alpha) = B(\beta, \alpha) + D(\beta, \alpha) + R(\beta, \alpha) \quad (20.27)$$

20.5.3.1 Direct irradiance

Straightforward geometrical considerations lead to

$$B(\beta, \alpha) = B \max(0, \cos \theta_s) \quad (20.28)$$

where B is the direct irradiance falling on a surface perpendicular to the sun's rays, and $\cos \theta_s$ is the angle of incidence between the sun's rays and the normal to the surface, given by equation (20.9). B can be obtained from the corresponding value on a horizontal surface

$$B = \frac{B(0)}{\cos \theta_{zs}} \quad (20.29)$$

Note that when the sun is illuminating the back of the surface (for example, during all morning on a vertical surface oriented to the west) $|\theta_s| > \pi/2$. Then, $\cos \theta_s < 0$ and $B = 0$. This way, the factor $\max(0, \cos \theta_s)$ reflects that the irradiance incident on the back surface of PV modules is normally not utilised.

20.5.3.2 Diffuse irradiance

We can assume that, when the sun is occulted, the sky is composed of elemental solid angles, such as $d\Omega$ (Figure 20.14) from which a diffuse radiance $L(\theta_z, \psi)$ is emanated towards the horizontal surface. The term radiance is taken to mean the flux of energy per unit solid angle crossing a surface normal to the direction of the radiation. It is expressed in $\text{W/m}^2 \cdot \text{steradian}$.

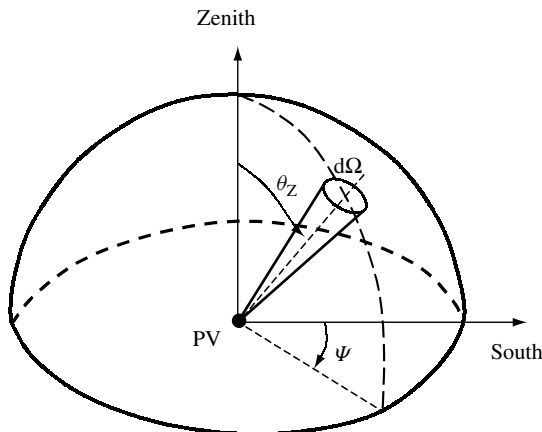


Figure 20.14 Angular co-ordinates, θ_z and ψ , of an elemental solid angle of the sky

Then, the horizontal irradiance is equal to the integration of the contribution of each solid angle, and can be written as

$$D(0) = \int_{\text{sky}} L(\vartheta_Z, \psi) \cos \vartheta_Z d\Omega \quad (20.30)$$

where the integral is extended to the whole sky, that is, $0 \leq \theta_Z \leq \pi/2$ and $0 \leq \psi \leq 2\pi$.

When we are dealing with an inclined surface, a similar reasoning leads to

$$D(\beta, \alpha) = \int_{\alpha} L(\vartheta_Z, \psi) \cos \vartheta'_Z d\Omega \quad (20.31)$$

where ϑ'_Z is the incident angle from the solid angle element to the inclined surface, and α means the integral is extended to the non-obstructed sky. The general solution of this equation is difficult because, under realistic skies, the radiance is not uniform and varies with the sky condition. For example, the form, brightness and position of clouds strongly affect the directional properties of the radiance.

The distribution of radiance over the sky is not measured routinely. Nevertheless, a number of authors [25, 26] have developed instruments to measure it and have presented results for different sky conditions. Some general patterns may be discerned from these.

With clear skies, the maximum diffuse radiance comes from the parts of the sky close to the sun and to the horizon. The minimum radiances come from a region at an angle of 90° to the solar zenith (Figure 20.15). The diffuse radiation coming from the region close to the sun is called *circumsolar radiation* and is mainly due to the dispersion by aerosols. The angular extent of the sun's aureole depends mainly on the turbidity of

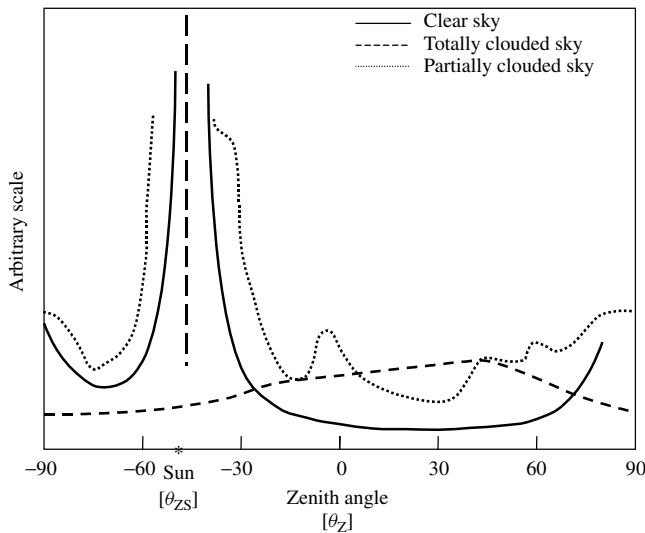


Figure 20.15 Typical angular distribution of the sky irradiance. The values are taken along the length of the meridian containing the sun, $\psi = \psi_S$

the atmosphere and on the zenith angle of the sun. The increase in diffuse radiance near the horizon is due to the albedo radiation of the Earth and is called *horizon brightening*.

The radiance distributions associated with overcast skies are very well described by Kondratyev: “for dense non-transparent cloudiness, the azimuthal dependence of diffuse radiation intensity is very weak. There is a slight monotonic increase of the radiance from the horizon upward towards the zenith” [27].

Some models can be derived from these general ideas. The simplest model makes use of the assumption that the sky radiance is isotropic, that is, every point of the celestial sphere emits light with equal radiance, $L(\theta_Z, \psi) = \text{constant}$. The solution of equations (20.30 and 20.31) leads then to

$$D(\beta, \alpha) = D(0) \frac{1 + \cos \beta}{2} \quad (20.32)$$

Because of its simplicity, this model has achieved great popularity, despite the fact that it systematically underestimates diffuse irradiance on surfaces tilted to the equator.

The opposite approach assumes that all the diffuse radiation is circumsolar, that is, from the sun. This is really a case of treating diffuse radiation as though it were direct, and leads to

$$D(\beta, \alpha) = \frac{D(0)}{\cos \theta_{ZS}} \max(0, \cos \theta_S) \quad (20.33)$$

This model also has the advantage of being very simple to use, but in general it overestimates diffuse irradiances.

In general, better results are obtained with so called anisotropic models. Hay and Davies [28] proposed to consider the diffuse radiation as composed by a circumsolar component coming directly from the direction of the sun, and an isotropic component coming from the entire celestial hemisphere. Both components are weighted according to the so-called anisotropy index, k_1 , defined as

$$k_1 = \frac{B(0)}{B_0(0)} = \frac{B}{B_0 \varepsilon_0} \quad (20.34)$$

The solution of equation (20.31) is now

$$D(\beta, \alpha) = D^I(\beta, \alpha) + D^C(\beta, \alpha) \quad (20.35)$$

where

$$D^I(\beta, \alpha) = D(0)(1 - k_1) \frac{1 + \cos \beta}{2} \quad (20.36)$$

and

$$D^C(\beta, \alpha) = \frac{D(0)k_1}{\cos \theta_{ZS}} \max(0, \cos \theta_S) \quad (20.37)$$

respectively, define the contribution of the isotropic and of the circumsolar components.

Note that k_1 is just the ratio between a pyrheliometer's reading and the solar constant, once corrected by the eccentricity due to the ecliptic orbit of the Earth around the sun. This way, k_1 can be understood as a measure of the instantaneous atmospheric transmittance for direct irradiance. When the sky is completely clouded over, $k_1 = 0$ and the above equation becomes the same as that for the simple isotropic model. This anisotropic model is an excellent compromise between simplicity and precision. It has been well-validated against measurements performed at different worldwide locations, and has been extensively used, for example, for the elaboration of the European Atlas of the Solar Radiation [9].

Also, very commonly employed, in particular with digital machines, is the model that has been put forward by Perez [29, 30]. It divides the sky into three zones acting as diffuse radiation sources: a circumsolar region, a horizontal band and the rest of the celestial hemisphere. The relative contributions of each component is modulated by means of empirical factors determined from the study of data from 18 measurement stations at 15 sites in North America and Europe. The Perez model used to perform slightly better than others [31], because the larger number of modulating factors allows for the consideration of a larger number of different sky conditions.

20.5.3.3 Albedo irradiance

The reflectivity of most types of ground is rather low. Consequently, the contribution of the albedo irradiance falling on a receiver is generally small. (An exception occurs in the case of snow.) There is therefore no point in developing very sophisticated models for albedo. It is usual to assume that the ground is horizontal and of infinite extent and that it reflects isotropically. On this basis, the albedo irradiance on an inclined surface is given by

$$R(\beta, \alpha) = \rho G(0) \frac{1 - \cos \beta}{2} \quad (20.38)$$

where ρ is the reflectivity of the ground and depends on the composition of the ground. When the value of ρ is unknown, it is common to take $\rho = 0.2$

It is now opportune to go forward with the example of the previous section, by calculating the irradiance components over a surface tilted to the latitude, the 15 April in Portoalegre-Brazil. Using equations (20.34) to (20.37) to deal with diffuse radiation and $\rho = 0.2$, the results, expressed in W/m^2 , are as follows:

| ω | k_1 | $D^I(\phi)$ | $D^C(\phi)$ | $B(\phi)$ | $R(\phi)$ | $G(\phi)$ |
|----------------|--------|-------------|-------------|-----------|-----------|-----------|
| ω_s | 0 | 0 | 0 | 0 | 0 | 0 |
| $\pm 60^\circ$ | 0.2205 | 73.40 | 31.80 | 147.56 | 2.73 | 255.49 |
| $\pm 30^\circ$ | 0.3082 | 124.14 | 76.94 | 357.14 | 6.26 | 564.48 |
| 0° | 0.3403 | 138.97 | 98.09 | 455.31 | 7.80 | 700.18 |

It becomes clear that the albedo can be generally neglected in PV calculations.

20.5.3.4 Daily irradiation

The most accurate way of calculating $G_{dm}(\beta, \alpha)$ from $G_{dm}(0)$ is, first, to calculate the hourly horizontal irradiation components $G_{hm}(0)$, $D_{hm}(0)$ and $B_{hm}(0)$; second, to transpose them to the inclined surface $G_{hm}(\beta, \alpha)$, $D_{hm}(\beta, \alpha)$ and $B_{hm}(\beta, \alpha)$; and, finally, to integrate during the day.

Such a procedure, summarised in Figure 20.16, allows us to account for the anisotropic properties of diffuse radiation, and leads to good results whatever the orientation of the inclined surface. However, it is laborious to apply and a computer must be used. It is interesting to mention that, for the case of surfaces tilted to the equator ($\alpha = 0$), frequently encountered in photovoltaic applications, if the diffuse radiation is taken to be isotropic, the following expression may be applied

$$G_d(\beta, 0) = B_d(0) \times RB + D_d(0) \frac{1 + \cos \beta}{2} + \rho G_d(0) \frac{1 - \cos \beta}{2} \quad (20.39)$$

where the factor RB represents the ratio between the daily direct irradiations on an inclined surface and on an horizontal surface, and may be approximated by setting it equal to the corresponding ratio between daily extraterrestrial irradiations on similar surfaces. Hence, RB is given as follows:

$$RB = \frac{\omega_{SS} \frac{\pi}{180} [\sin(\phi)] \sin \delta \sin(|\phi| - \beta) + \cos \delta \cos(|\phi| - \beta) \sin \omega_{SS}}{\omega_S \frac{\pi}{180} \sin \delta \sin \phi + \cos \delta \cos \phi \sin \omega_S} \quad (20.40)$$

where ω_{SS} is the sunrise angle on the inclined surface, which is given by

$$\omega_{SS} = \max[\omega_S, -\arccos(-[\sin(\phi)] \tan \delta \tan(abs(\phi) - \beta))] \quad (20.41)$$

It is interesting to observe that for the equinox days, $\delta = 0 \Rightarrow \omega_S = \omega_{SS}$ and equation (20.40) becomes $RB = \cos[abs(\phi) - \beta] / \cos \phi$.

Example: Estimate the average daily irradiation in January at Changchun–China ($\phi = 43.8^\circ$) over a fixed surface facing south and tilted at an angle $\beta = 50^\circ$ with respect to the horizontal, knowing that the mean value of the global horizontal irradiation is $G_{dm}(0) = 1861 \text{ Wh/m}^2$ and the ground reflection $\rho = 0.2$. The solution is as follows:

$$\text{January} \Rightarrow d_n = 17; \delta = -20.92^\circ$$

$$\phi = 43.8^\circ \Rightarrow \omega_S = -68.50 \text{ and } B_{0d}(0) = 3586 \text{ Wh/m}^2 \Rightarrow K_{Tm} = 0.519$$

$$\Rightarrow F_{Dm} = 0.414$$

$$D_{dm}(0) = 770 \text{ Wh/m}^2; B_{dm}(0) = 1091 \text{ Wh/m}^2$$

$$\arccos(-\tan \delta \tan(\phi - \beta)) = -92.38^\circ \Rightarrow \omega_{SS} = -68.5^\circ \Rightarrow RB = 2.741$$

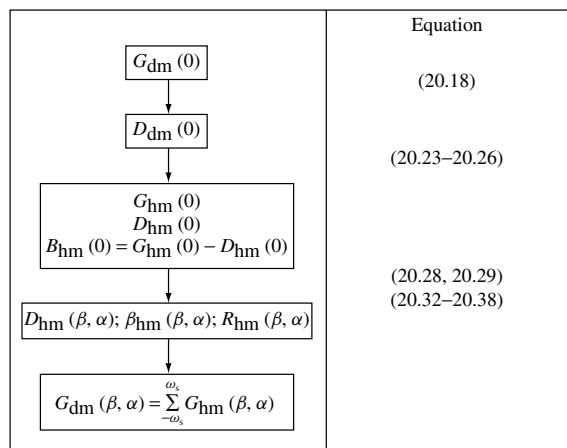


Figure 20.16 Diagram explaining the calculation of the daily irradiation on an inclined surface $G_{dm}(\beta, \alpha)$ from the corresponding horizontal value $G_{dm}(0)$

$$D_{dm}(50) = 633 \text{ Wh/m}^2; B_{dm}(50) = 2990 \text{ Wh/m}^2; R_{dm}(50) = 66 \text{ Wh/m}^2$$

$$G_{dm}(50) = 3689 \text{ Wh/m}^2$$

It is worth mentioning that a more detailed calculation, following the procedure outlined in Figure 20.16, would lead to $G_{dm}(50) = 3956 \text{ Wh/m}^2$. That means the error associated to equation (20.40) is below 8%. This difference is mainly due to the different consideration of the diffuse radiance distribution.

20.6 DIURNAL VARIATIONS OF THE AMBIENT TEMPERATURE

The behaviour of the photovoltaic modules depends, to some extent, on the ambient temperature. Just as it is for solar radiation, sometimes it is necessary to determine how this parameter varies throughout the day. The data available as a starting point for this calculation are, in general, the maximum and minimum temperature of the day, T_{aM} and T_{am} , respectively.

A model that is simple but, nevertheless, gives a good fit to the experimental values is obtained from the fact that the temperature evolves in a similar manner to the global radiation but with a delay of about 2 h. This fact allows the following three principles to be deduced

- T_{am} occurs at sunrise ($\omega = \omega_s$).
- T_{aM} occurs two hours after midday ($\omega = 30^\circ$).
- Between these two times, the ambient temperature develops according to two semi cycles of a cosine function: one from dawn to midday, and the other between midday and sunrise of the following day.

The following set of equations based on the above, permits the ambient temperature throughout a day j to be calculated as follows:

For $-180 < \omega \leq \omega_S$

$$T_a(j, \omega) = T_{aM}(j-1) - \frac{T_{aM}(j-1) - T_{am}(j)}{2} [1 + \cos(a\omega + b)] \quad (20.42)$$

with $a = \frac{-180}{\omega_S + 330}$ and $b = -a\omega_S$

For $\omega < \omega_S \leq 30$

$$T_a(j, \omega) = T_{am}(j) + \frac{T_{aM}(j) - T_{am}(j)}{2} [1 + \cos(a\omega + b)] \quad (20.43)$$

with $a = \frac{180}{\omega_S - 30}$ and $b = -30a$

For $30 < \omega \leq 180$

$$T_a = T_{aM}(j) - \frac{T_{aM}(j) - T_{am}(j+1)}{2} [1 + \cos(a\omega + b)] \quad (20.44)$$

with $a = \frac{180}{\omega_S + 330}$ and $b = -(30a + 180)$

To apply these equations, it is necessary to know the maximum temperature on the previous day, $T_{aM}(j-1)$, and the minimum temperature of the following day, $T_{am}(j+1)$. If these data are unavailable, then it can be assumed, without introducing too much error, that they equal those for the day in question.

20.7 EFFECTS OF THE ANGLE OF INCIDENCE AND OF THE DIRT

The reflectance and transmittance of optical materials depends on the angle of incidence. Glass covers of solar collectors are not an exception and therefore the optical input of photovoltaic modules is affected by their orientation with respect to the sun, due to the angular variation of the glass reflection. Theoretical models, based on the well-known Fresnel formulae, have been developed for clean surfaces. The most popular formulation is from ASHRAE [32]. For a given incidence angle, θ_S , it can be described by the simple expression

$$FT_B(\theta_S) = 1 - b_0 \left(\frac{1}{\cos \theta_S} - 1 \right) \quad (20.45)$$

where $FT_B(\theta_S)$ is the relative transmittance, normalised by the total transmittance for normal incidence, and b_0 is an adjustable parameter that can be empirically determined for each type of photovoltaic module. If this value is unknown, a general value $b_0 = 0.07$ may be used. The effect of the angle of incidence on the successfully collected solar radiation can be calculated by applying equation (20.45) to the direct and circumsolar irradiances, and by considering an approximated value, $FT = 0.9$, for the isotropic diffuse and reflected radiation terms. Figure 20.17 shows a plot of $FT_B(\theta_S)$ versus θ_S . It presents

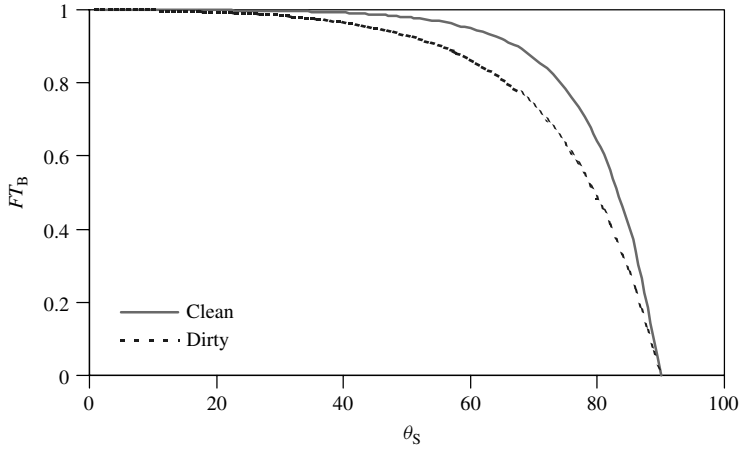


Figure 20.17 The relative transmittance FT_B is plotted against the angle of incidence θ_S , for a clean surface and also for a dust-covered surface

a pronounced knee close to 60° . In practical terms, that means the effects of the angle of incidence are negligible for all the θ_S values well below this figure. For example, $FT_B(40^\circ) = 0.98$.

The ASHRAE model is simple to use but has noticeable disadvantages. It cannot be used for $\theta_S > 80^\circ$, and, still worse, it cannot take into consideration the effects of dust. Dust is always present in real situations, and not only reduces the transmittance at normal incidence but also influences the shape of $FT_B(\theta_S)$. Figure 20.17 shows that the relative transmittance decreases because of dust at angles from about 40 to 80° . Real $FT_B(\theta_S)$ are best described [33] by

$$FT_B(\theta_S) = 1 - \frac{\exp\left(-\frac{\cos \theta_S}{a_r}\right) - \exp\left(-\frac{1}{a_r}\right)}{1 - \exp\left(-\frac{1}{a_r}\right)} \quad (20.46)$$

where a_r is an adjust parameter mainly associated with the degree of dirtiness, as shown in Table 20.4. Note that the degree of dirtiness is characterised by the corresponding relative normal transmittance, $T_{\text{dirt}}(0)/T_{\text{clean}}(0)$. Equation (20.46) applies for direct and circumsolar radiation components. The angular losses for isotropic diffuse and albedo radiation components are, respectively, approximated by [33]

$$FT_D(\beta) = 1 - \exp \left[-\frac{1}{a_r} \left[c_1 \left(\sin \beta + \frac{\pi - \beta \cdot \frac{\pi}{180} - \sin \beta}{1 + \cos \beta} \right) + c_2 \left(\sin \beta + \frac{\pi - \beta \cdot \frac{\pi}{180} - \sin \beta}{1 + \cos \beta} \right)^2 \right] \right] \quad (20.47)$$

Table 20.4 Recommended parameters for angular losses calculation

| Dirtiness degree | $T_{\text{dirt}}(0)/T_{\text{clean}}(0)$ | a_r | c_2 |
|------------------|--|-------|--------|
| Clean | 1 | 0.17 | -0.069 |
| Low | 0.98 | 0.20 | -0.054 |
| Medium | 0.97 | 0.21 | -0.049 |
| High | 0.92 | 0.27 | -0.023 |

and

$$FT_R(\beta) = 1 - \exp \left[-\frac{1}{a_r} \left[c_1 \left(\sin \beta + \frac{\beta \cdot \frac{\pi}{180} - \sin \beta}{1 - \cos \beta} \right) + c_2 \left(\sin \beta + \frac{\beta \cdot \frac{\pi}{180} - \sin \beta}{1 - \cos \beta} \right)^2 \right] \right] \quad (20.48)$$

where $c_1 = 4/(3\pi)$ and c_2 is linearly related to a_r . Table 20.4 also presents some values of these parameters for several dirtiness degrees.

It must be noted that $FT_B(0) = 1$. That means, this function does not include the dirt effect on the relative normal transmittance but only the angular losses relative to normal incidence. In other words, the “effective” direct irradiance reaching the solar cells of a PV module, should be computed as

$$B_{\text{eff}}(\beta, \alpha) = B(\beta, \alpha) \times \frac{T_{\text{dirt}}(0)}{T_{\text{clean}}(0)} \times FT_B(\theta_S) \quad (20.49)$$

and similar expressions should be used for the diffuse and albedo irradiance (or hourly irradiation) components.

Following the example of 15 April in Portoalegre-Brazil, we can now calculate the effective irradiances over a surface tilted to the latitude, neglecting the albedo, supposing a medium dirtiness degree and by applying $FT_B(\theta_S)$ not only to the direct radiation but also to the circumsolar component of the diffuse radiation. Obviously, $FT_D(\beta)$ is applied to the isotropic component of the diffuse radiation. The results are as follows:

$$FT_D(\phi) = 0.934$$

| ω° | $FT_B(\theta_S)$ | $B_{\text{eff}}(\phi)$, [Wm ⁻²] | $D_{\text{eff}}(\phi)$ [Wm ⁻²] | $G_{\text{eff}}(\phi)$ [Wm ⁻²] | ΔG_{eff} [%] |
|----------------|------------------|---|---|---|--------------------------------|
| ω_S | 0 | 0 | 0 | 0 | 0 |
| ± 60 | 0.913 | 80.84 | 126.39 | 207.23 | -11.3 |
| ± 30 | 0.991 | 249.63 | 249.74 | 499.37 | -6.8 |
| 0 | 0.999 | 332.13 | 296.37 | 628.50 | -6.1 |

The last column of this table describes the losses due to both dirt and angular effects. Taking into consideration that dirt reduces normal transmittance by a factor of 3% ($T_{\text{dirt}}(0)/T_{\text{clean}}(0) = 0.97$), it can be noted that pure angular losses dominate for $|\omega| > 30^\circ$.

Finally, it should be stressed that angular-dependent reflection is often neglected in PV simulations. However, they become significant in many practical situations, for example, where vertical (façade-integrated PV generators) or horizontal (N–S horizontal trackers) surfaces are concerned. Furthermore, they help to explain the observed low irradiance effects in PV module performance. This is because low irradiance just happens when the incidence angle is large or when solar radiation is mainly diffuse. In both cases, angular losses are particularly important. As a matter of fact, the failure to consider angular losses has been signalled as the main cause of error in some energy models [34].

20.8 SOME CALCULATION TOOLS

20.8.1 Generation of Daily Radiation Sequences

Long series (many years) of daily irradiation data are sometimes required for particular purposes, for example, when studying the long-term reliability of stand-alone photovoltaic systems. However, long series of historical data are scarce and hard to obtain. This leads to the need for methods that are able to generate a series starting from widely available information, such as the 12 long-term average monthly mean values of the daily irradiation, $G_{\text{dm}}(0)$. The idea is that the generated series must keep some statistical properties believed to be universal, as they are also found in historical data, when available. In particular, the persistence of solar radiation, that is, the dependence of today's irradiation on the irradiation of the precedent days, is adequately described by a first-order autoregressive process [35]. Moreover, the probability function of the daily clearness index for any given period has a form associated with only its average value for the period. Several methods for the generation of daily irradiation sequences are available in the literature [36]. The method proposed by Aguiar [37] is the most widely used today.

20.8.2 The Reference Year

As already mentioned, the most widely available information related to the solar radiation resource at a given location is the set of 12 monthly mean values of global horizontal daily irradiation, $G_{\text{dm}}(0)$. The methods presented above allow estimation of all the radiation components incident on any surface of arbitrary orientation and at any moment of the average year, and even at any moment of a long sequence of years. This can be applied to all the problems related to the design of photovoltaic systems: sizing, prediction of energy yields, impact of shadowing, optimisation of tilt angles and so on.

Nevertheless, the solar radiation is still the object of systematic recording, and more and more irradiance and irradiation data are being accumulated and put at public disposal. Such data whether in the form of crude recorded data or in the form of elaborate mathematical tools, attempt to properly represent the climate of the concerned location. The most widely used is the so-called Reference Year, also called the Typical Meteorological Year [18], *TMY*, or the Standard Year. The *TMY* for a location is a hypothetical

year in which months are real months, but are chosen from different years from the whole period for which data are available. In practice [38], the months are chosen such that the monthly mean of the daily global irradiation on the horizontal represents an average value for all values contained in the database. For example, January of 1986 was chosen for the *TMY* of Madrid, because it had a value of $G_{dm}(0) = 1.98 \text{ kWh/m}^2$, the closest to the average value of $G_{dm}(0) = 1.99 \text{ kWh/m}^2$ for all the months of January on record [16].

The most widely used *TMY* for photovoltaic applications is set in a one-hour time scale. Hence, it contains 4380^1 values of global horizontal irradiation. Ambient temperature values are also specified for each hour. This huge number of initial data can lead to the impression that the corresponding results should be much more accurate than those obtained when simply using the 12 $G_{dm}(0)$ values as input. However, this impression is largely wrong. On the one hand, because the representativeness of any data – it should be again remembered – is limited by the random nature of the solar radiation, small differences in the results are scarcely meaningful. On the other hand, because the results obtained from the 12 $G_{dm}(0)$ values and from the *TMY* are very similar, provided the initial data are coherent (i.e. the monthly means in the *TMY* coincides with the 12 $G_{dm}(0)$ values) and that the selected correlations and diffuse radiation models to transpose from horizontal to inclined surfaces are the same. The physical reasons for this lie in the quasi-linear power-irradiance relationship in most PV devices, and in the fact, initially shown by Liu and Jordan [19], that the solar climate of a particular location can be well characterised by only the monthly mean daily clearness index. As already mentioned, they have demonstrated that, irrespective of latitude, the fractional time during which daily global radiation is equal to or less than a certain value depends only on this parameter. Surely, to go into this question in-depth would increase the reader's boredom which is probably already large enough; hence, we will restrict ourselves to describing a representative case from our own experience:

In 1992, the Solar Energy Institute in the University of Madrid, IES-UPM, was involved in the design of the 1 MW PV plant in Toledo, Spain. It was the biggest European PV project at that time, so very careful studies were required at the initial project stage. Fortunately, a large historical database, containing 20 years of hourly irradiation data, was available from a nearby meteorological station, and was directly used to calculate the expected energy yields. Both static and sun-tracked photovoltaic arrays were analysed while taking into account detailed features such as shadowing from adjacent rows, back-tracking features and so on. Moreover, the same calculation was also performed using as input the *TMY*, previously derived from the historical radiation sequence, and also using as the only input the 12 $G_{dm}(0)$ values and computing for just the mean day of each month. The results from the three calculation procedures never differed more than 2%! As a matter of fact, the results were much more sensitive to the considerations of the solar angle of incidence effects [39] described below.

A clever friend, not involved in this project but being aware of this anecdote, posed the questions: Then why go into such exhaustive detail when they give similar results?

¹ There are 8760 hours per year, and the sun shines exactly half of the year in any location, hence there are 4380 hours of sunshine per year.

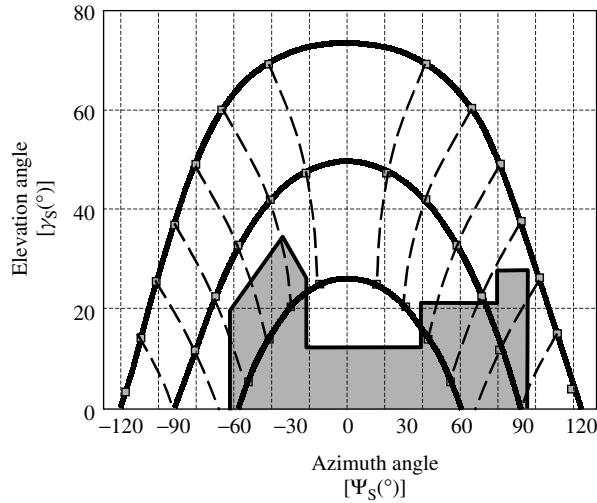


Figure 20.18 Sun's trajectory map corresponding to a latitude $\phi = 40.5^{\circ}$, with a skyscraper superimposed on the map. For example, on the winter solstice, shadows occur from sunrise to about 10:30 (solar time) and from 14:30 to sunset

Why not just be simple? The proper answers are best found in human psychology. Many people simply desire not to believe in some ideas. Hence, the ones daring to declare them are automatically impelled to provide strong arguments in favour of such ideas. To a large extent, this is usually the case when defending the argument that modern complex software tools do not necessarily yield better results than simple (but judicious) traditional methods. That was the position of the IES-UPM in 1992, and today for the author of this chapter the position remains the same.

20.8.3 Shadows and Trajectory Maps

Surroundings of photovoltaic modules can include trees, mountains, chimneys, walls, other PV modules and so on. Because of that, photovoltaic modules cannot always be positioned entirely free of shadows. This reduces their potential energy yield, and must be taken into account when designing photovoltaic systems. Equations (20.3 to 20.5) allow the plotting of the trajectories of the sun, in terms of elevation versus azimuth angles, as already explained in Figure 20.6.

These types of diagrams are called sun trajectory maps. They are a very useful tool for determining the duration and effect of shadowing cast by any obstacle. A correctly placed theodolite can measure the azimuth and elevation angles of the most relevant points (corners, peaks etc.) of any kind of obstacle. The *local horizon* can then be superimposed on the trajectory map, as Figure 20.18 shows. The effect of the shadow is calculated with the assumption that the direct and circumsolar radiations are zero when the sun is below the local horizon. Unless the shadows are very large, the effect of the local horizon on the diffuse radiation (other than the circumsolar component) can be neglected. Several tools have been proposed [40, 41] to simplify the practise of this calculation.

20.9 IRRADIATION ON MOST WIDELY STUDIED SURFACES

This section analyses some important features of the radiation available on commonly studied surfaces. As already mentioned, the methods presented before conform to a complete package, allowing the calculation of the irradiation incident over any arbitrary surface over any period of time, using the horizontal data as input. This can no doubt be a tedious task, so specific commercial software packages have been developed [42, 43]. However, for many practical engineering problems, more direct and simple tools can be developed. In particular, it is possible to develop analytical expressions that can be simply solved by only hand calculations. In order to apply the discussion in the previous sections, let us analyse the particular case of the yearly mean daily irradiation collected at four different places on a fixed surface, tilted towards the equator ($\alpha = 0$) and inclined at an angle β to the horizontal, $G_{dy}(\beta)$. Figure 20.19 plots, for each place, such value in relation to its maximum and versus the inclination angle referred to as the absolute value of the latitude, that is, $G_{dy}(\beta - |\phi|)/G_{dy}(\beta_{opt})$, being β_{opt} the inclination angle associated to the maximum value of $G_{dy}(\beta)$. The calculation procedure had followed the lines described in Figure 20.16. Solar radiation data has been obtained from Reference [7]. Several aspects need to be outlined.

On the one hand, a great similarity between all the curves is noticeable. Despite large differences in latitude and clearness index of the selected locations, the shape of the curve and also the inclination angle maximising the collection of radiation are very similar for the four selected places. Furthermore, this angle is relatively close to the latitude. It is important to mention that the extension of this exercise to many other places all around the world verifies that this great similarity is nearly universal. In fact, we have performed a specific exercise covering 30 different places distributed from $\phi = 80^\circ$ to $\phi = -78.2^\circ$ (see list in Table 20.5). We limit Figure 20.19 to only four curves for presentation purposes. A physical explanation of this similitude can be argued observing that, irrespective of the latitude, all the surfaces tilted towards the equator and inclined at an angle equal to the absolute value of the latitude are parallel all over the Earth, and also parallel to the Earth's rotation axis. Therefore, in the absence of the atmosphere, on

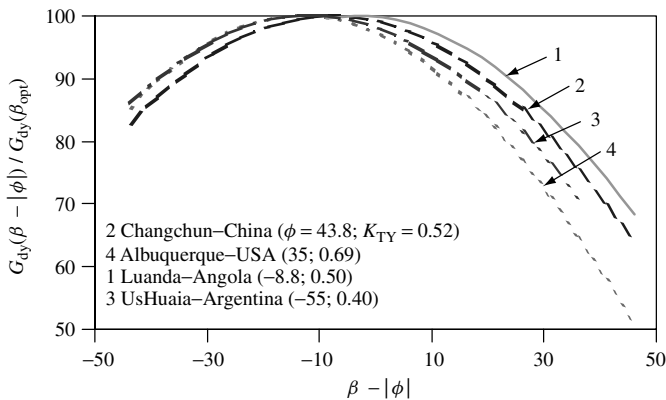


Figure 20.19 Yearly energy collection versus inclination angle for surfaces tilted towards the equator. The percentage of relative collection, with respect to the maximum, $G_{dy}(\beta - |\phi|)/G_{dy}(\beta_{opt})$ is plotted against the difference between the tilt angle and the latitude $\beta - |\phi|$

Table 20.5 Annual radiation availability on different surfaces, for 30 different places all around the world. Various tracking options (1 axis, 2 axis, etc.) described in Section 20.9.2

| Location | Lat. ϕ° | $B_{0dy}(0)$ [Wh/m ²] | Clearness index K_{Ty} | Ratios to global horizontal yearly irradiation | | | | | |
|-------------------------|----------------------|--------------------------------------|--------------------------------|--|-----------|-----------|-----------|------------------------|-----------------|
| | | | | 2 axis | 1 Az-axis | 1 Ho-axis | 1 Po-axis | Fixed β_{opt} | 2 axis Conc. |
| Ice-Island-Arctic | 80 | 4261 | 0.580 | 2.75 | 2.54 | 1.97 | 2.60 | 1.67 | 2.26 |
| S. Petersburg-Russia | 59.9 | 5703 | 0.453 | 1.72 | 1.64 | 1.43 | 1.61 | 1.18 | 1.21 |
| Hamburg-Germany | 53.6 | 6437 | 0.412 | 1.49 | 1.42 | 1.28 | 1.39 | 1.11 | 0.97 |
| Freiburg-Germany | 48 | 7075 | 0.428 | 1.42 | 1.36 | 1.26 | 1.33 | 1.07 | 0.93 |
| Nantes-France | 47.2 | 7164 | 0.468 | 1.50 | 1.44 | 1.31 | 1.41 | 1.10 | 1.03 |
| Olympia-USA | 46.6 | 7230 | 0.437 | 1.41 | 1.35 | 1.27 | 1.32 | 1.05 | 0.93 |
| Changchun-China | 43.8 | 7531 | 0.510 | 1.60 | 1.53 | 1.35 | 1.51 | 1.16 | 1.13 |
| Sapporo-Japan | 43 | 7615 | 0.421 | 1.41 | 1.35 | 1.22 | 1.31 | 1.09 | 0.89 |
| Madrid-Spain | 40.4 | 7880 | 0.544 | 1.53 | 1.46 | 1.36 | 1.45 | 1.08 | 1.12 |
| Seoul-Korea | 37.5 | 8161 | 0.440 | 1.39 | 1.32 | 1.23 | 1.30 | 1.07 | 0.89 |
| Albuquerque-USA | 35 | 8391 | 0.687 | 1.66 | 1.55 | 1.47 | 1.58 | 1.09 | 1.37 |
| Djelfa-Algeria | 34.6 | 8427 | 0.584 | 1.53 | 1.44 | 1.45 | 1.37 | 1.06 | 1.15 |
| El Paso-Mexico | 31.5 | 8691 | 0.689 | 1.61 | 1.49 | 1.45 | 1.53 | 1.07 | 1.33 |
| Shanghai-China | 31.2 | 8716 | 0.487 | 1.36 | 1.29 | 1.25 | 1.27 | 1.02 | 0.91 |
| Cairo-Egypt | 30.6 | 8764 | 0.637 | 1.53 | 1.43 | 1.39 | 1.46 | 1.05 | 1.20 |
| Delhi-India | 28.6 | 8919 | 0.630 | 1.56 | 1.44 | 1.40 | 1.47 | 1.07 | 1.23 |
| Karachi-Pakistan | 24.8 | 9189 | 0.560 | 1.48 | 1.36 | 1.35 | 1.39 | 1.04 | 1.13 |
| Morelia-Mexico | 19.7 | 9494 | 0.415 | 1.20 | 1.14 | 1.14 | 1.08 | 0.98 | 0.70 |
| Dakar-Senegal | 14.7 | 9729 | 0.599 | 1.38 | 1.23 | 1.31 | 1.29 | 0.98 | 1.04 |
| Bangkok-Thailand | 13.7 | 9768 | 0.490 | 1.27 | 1.16 | 1.21 | 1.14 | 0.98 | 0.83 |
| Claveria-Philippines | 8.6 | 9924 | 0.513 | 1.27 | 1.13 | 1.23 | 1.16 | 0.95 | 0.86 |
| Colombo-Sri Lanka | 6.9 | 9961 | 0.529 | 1.28 | 1.12 | 1.23 | 1.16 | 0.96 | 0.76 |
| Medellin-Colombia | 6.2 | 9974 | 0.469 | 1.22 | 1.08 | 1.18 | 1.08 | 0.95 | 0.76 |
| Luanda-Angola | -8.8 | 9918 | 0.497 | 1.26 | 1.12 | 1.21 | 1.13 | 0.95 | 0.83 |
| El Alto-Bolivia | -16.4 | 9652 | 0.579 | 1.39 | 1.25 | 1.31 | 1.29 | 0.99 | 1.04 |
| Sao Paulo-Brazil | -23.5 | 9267 | 0.427 | 1.25 | 1.19 | 1.17 | 1.14 | 0.99 | 0.76 |
| Porto Alegre-Brazil | -30 | 8805 | 0.505 | 1.38 | 1.30 | 1.26 | 1.29 | 1.02 | 0.93 |
| Bariloche-Argentina | -41.1 | 7801 | 0.566 | 1.58 | 1.50 | 1.40 | 1.50 | 1.07 | 1.18 |
| Ushuaia-Argentina | -55 | 6263 | 0.402 | 1.62 | 1.55 | 1.30 | 1.51 | 1.19 | 1.07 |
| Little America-Antartic | -78.2 | 4306 | 0.577 | 2.67 | 2.48 | 1.87 | 2.52 | 1.55 | 2.12 |

the equinox days, they receive identical solar irradiation, $B_{0d}(|\phi|)|_{\delta=0}$. And the same is true for surfaces equally tilted with respect to the latitude angle, $B_{0d}(\beta - |\phi|)|_{\delta=0}$. For other than equinox days, this is not exactly true, because sunrise time (and, therefore, the length of daytime and, in turn, the daily extraterrestrial irradiation) depends on latitude, as described by equation (20.7). However, the yearly ratio between extraterrestrial irradiation collected on both inclinations, $B_{0dy}(\beta - |\phi|)/B_{0dy}(|\phi|)$ tends to remain constant. Now, when accounting for the Earth's atmosphere, such site independence is not necessarily maintained, because of the different climatic conditions, that is, the different annual clearness index K_{Ty} , from one site to another. Obviously, the collection of diffuse radiation is less sensitive to inclination angle variations than the collection of direct radiation. Because of this, the lower the K_{Ty} value (the higher the F_{dy}), the slightly less is sharp-pointed curve that should be expected. Figure 20.19 reveals that this tendency is, in fact, very weak, so that the site independence clearly dominates and the function $G_{dy}(\beta - |\phi|)/G_{dy}(\beta_{opt})$ can be properly considered as being a universal invariant.

On the other hand, the smooth form of the curves of Figure 20.19 suggests that it may be possible to describe them analytically, thus avoiding the need to use a computer each time a particular value is required. A convenient way of doing it is, first, analysing the correspondence between the optimal inclination angle and latitude. It is worth noting that the larger the latitude, the larger the difference between summer daytime and winter daytime and, in turn, the larger the difference between the summer and the winter irradiation. Therefore, it can be anticipated that as latitude increases, the optimal inclination angle should progressively give priority to the collection of summer over the collection of winter. This can be observed in Figure 20.20, where the values of $\beta_{\text{opt}} - |\phi|$ have been plotted against the latitude, for the 30 above-mentioned different locations.

It is useful to fit a linear equation to these values

$$\beta_{\text{opt}} - |\phi| = 3.7 - 0.31|\phi| \quad \text{or} \quad \beta_{\text{opt}} = 3.7 + 0.69|\phi| \quad (20.50)$$

where β and ϕ are given in degrees. It is worth mentioning that the observed dispersion of the cluster of points around equation (20.50) (also depicted in Figure 20.20) is, in fact, of negligible importance, due to the very low sensibility of the energy collection to deviations from the optimal inclination angle. For example, the point corresponding to Delhi ($\phi = 28.6^\circ$) – marked as ♥ in the figure – indicates a value of $\beta_{\text{opt}} = 29.6^\circ$, while equation (20.50) leads to $\beta_{\text{opt}} = 23.4^\circ$. The 6.2° of difference can appear relatively large ($\approx 20\%$), but a detailed simulation exercise would disclose that $G_{\text{dy}}(23.4^\circ)/G_{\text{dy}}(29.6^\circ)$ is 99%, that is, such a difference is irrelevant when translated into energy content. A similar reasoning also justifies the validity of the usual assumption $\beta_{\text{opt}} = \phi$. Now, a second-order polynomial describes very well the curves of Figure 20.19.

$$\frac{G_{\text{dy}}(\beta)}{G_{\text{dy}}(\beta_{\text{opt}})} = 1 + p_1(\beta - \beta_{\text{opt}}) + p_2(\beta - \beta_{\text{opt}})^2 \quad (20.51)$$

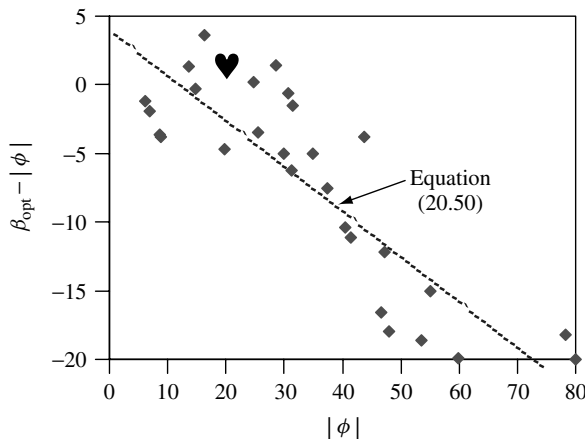


Figure 20.20 Optimal inclination angle versus latitude. The difference between $\beta_{\text{opt}} - |\phi|$ is plotted against the latitude $|\phi|$. The cluster of points corresponds to the different places listed in Table 20.5

where p_1 and p_2 are the adjusted parameters for which values are 4.46×10^{-4} and -1.19×10^{-4} , respectively. The corresponding value of the so-called correlation coefficient, R^2 , is greater than 0.98, indicating that equations (20.50) and (20.51) adjust very well to the simulated values. This way, the results of a rather complex calculation, involving a lot of tedious steps, can be described by means of two simple mathematical expressions. Apart from simplicity and elegance, all the information has been condensed into just four numbers and an equation that have the advantage of having a continuous slope, which can be useful in many calculations. It is worth mentioning that these equations can also be used to calculate the value of $G_{dy}(\beta_{opt})$ from the data corresponding to the horizontal surface, which is the most usually available information.

Example: Estimation of the optimal tilt angle and the corresponding yearly irradiation in Sapporo-Japan knowing the latitude, $\phi = 43^\circ$, and the annual average of the daily global horizontal irradiation, $G_{dy}(0) = 3220 \text{ Wh/m}^2$. The solution is

$$\text{Equation (20.50), } \phi = 43^\circ \Rightarrow \beta_{opt} = 33.37^\circ$$

$$\text{Equation (20.51), } \beta = 0^\circ \Rightarrow G_{dy}(0)/G_{dy}(\beta_{opt}) = 0.8526$$

$$\Rightarrow G_{dy}(\beta_{opt}) = 1.1729 \times G_{dy}(0) = 3776 \text{ Wh/m}^2.$$

The total yearly irradiation is $365 \times G_{dy}(0) = 1379 \text{ kWh/m}^2$.

It is worth mentioning that a more careful calculation, using the 12 values of the monthly mean irradiation and following the procedure described in Figure 20.16, would lead to $G_{dy}(\beta_{opt}) = 3663 \text{ Wh/m}^2$. This means, that the error associated to equation (20.51) is below 3%.

Attempting to help in the following discussion, Table 20.5 presents the results of a detailed simulation exercise devoted to the calculation of the annual radiation availability on horizontal surfaces, optimally tilted fixed surfaces and several types of tracking surfaces. The exercise has been extended to 30 different places distributed around the World. The hope is that the readers could find here a relatively similar location, both in latitude and clearness index, to the location of their interest. The yearly means of the daily global horizontal irradiation, $G_{dy}(0)$, can be obtained by multiplying the corresponding values of the extraterrestrial radiation and the clearness index. (column 3 \times column 4). Then, these horizontal $G_{dy}(0)$ values are used as reference for the irradiation availability in all the other considered surfaces. In particular, column 8 of this table gives the ratio between the global irradiation on a fixed and optimally tilted surface to the global horizontal irradiation, $G_{dy}(\beta_{opt})/G_{dy}(0)$. Hence, the irradiation on the optimally tilted surface is given by the product (column 3 \times column 4 \times column 8).

20.9.1 Fixed Surfaces

The integration of PV generators in buildings, presently in vogue in many industrialised countries, led to the use of a large range of different orientations and tilt angles. PV module orientations from east to west, and tilt angles from horizontal to vertical are found in practise. Then, it is worth extending the previous exercise to surfaces other than those

tilted towards the equator, that is, to $\alpha \neq 0$, and also to dirty surfaces. E. Caamaño [44] has proposed the following solution:

$$\frac{G_{\text{effdy}}(\beta, \alpha)}{G_{\text{dy}}(\beta_{\text{opt}})} = g_1(\beta - \beta_{\text{opt}})^2 + g_2(\beta - \beta_{\text{opt}}) + g_3 \quad (20.52)$$

where

$$g_i = g_{i1} \cdot |\alpha|^2 + g_{i2} \cdot |\alpha| + g_{i3}; i = 1, 2, 3 \quad (20.53)$$

being the values of the coefficients as show in Table 20.6, for medium dirty surfaces. The sub-index “eff” in the left term of equation (20.52) indicates that the dirt effect on the relative normal transmittance is also being included, in order to facilitate the direct application of the equation to real cases.

Let us continue with the example of Sapporo-Japan, by calculating the effective irradiation available on the following surfaces:

1. Optimally oriented, $\alpha = 0$, and optimally tilted, $\beta = \beta_{\text{opt}}$
Equation (20.53), $\alpha = 0 \Rightarrow g_i = g_{i3}$
Equation (20.52), $\beta = \beta_{\text{opt}} \Rightarrow G_{\text{effdy}}(\beta_{\text{opt}}) = 0.9314 G_{\text{dy}}(\beta = \beta_{\text{opt}}) = 3517 \text{ Wh/m}^2$
Note that the total losses due to the optical effects of the angle of incidence ($\approx 7\%$) are larger than pure normal transmittance losses ($\approx 3\%$)
2. Tilted 20° with respect to the horizontal, $\beta = 20^\circ$, and oriented 30° towards the west, $\alpha = 30^\circ \Rightarrow g_1 = -1.032 \times 10^{-4}$; $g_2 = 1.509 \times 10^{-4}$; $g_3 = 0.9057$
 $\beta - \beta_{\text{opt}} = -13.37^\circ \Rightarrow G_{\text{effdy}}(20, 30) = 0.8853 \cdot G_{\text{dy}}(\beta_{\text{opt}}) = 3343 \text{ Wh/m}^2$
It is worth mentioning that a similar calculation, but without considering the angular losses, would lead to $G_{\text{dy}}(20, 30) = 0.936 \cdot G_{\text{dy}}(\beta_{\text{opt}}) = 3533 \text{ Wh/m}^2$
3. A vertical facade, $\beta = 90^\circ$, oriented towards the south-east, $\alpha = -45^\circ$.
 $\alpha = -45^\circ \Rightarrow g_1 = -0.885 \times 10^{-4}$; $g_2 = -2.065 \times 10^{-4}$; $g_3 = 0.8761$
 $\beta - \beta_{\text{opt}} = 56.63^\circ \Rightarrow G_{\text{effdy}}(90, -45) = 0.5806 \cdot G_{\text{dy}}(\beta_{\text{opt}}) = 2192 \text{ Wh/m}^2$

It is opportune to mention again the relatively weak sensitivity of the annual capture of energy to the inclination angle. A value of 0.2% loss for each degree of deviation from the optimum value is a rough approximation. This is true to an even greater extent in the case of azimuthal orientation, where only a 0.08% loss occurs for each degree of deviation from the south. This means that many existing surfaces (roofs, car parks etc.) are suitable for PV modules integration, even if their orientation differs considerably from

Table 20.6 Coefficients used to solve equation (20.52). Values are given for the representative case of medium dirtiness degree ($T_{\text{dirt}}(0)/T_{\text{clean}}(0) = 0.97$)

| Coefficients | $T_{\text{dirt}}(0)/T_{\text{clean}}(0) = 0.97$ | | |
|--------------|---|-------------------------|-------------------------|
| | $i = 1$ | $i = 2$ | $i = 3$ |
| g_{1i} | 8×10^{-9} | 3.8×10^{-7} | -1.218×10^{-4} |
| g_{2i} | -4.27×10^{-7} | 8.2×10^{-6} | 2.892×10^{-4} |
| g_{3i} | -2.5×10^{-5} | -1.034×10^{-4} | 0.9314 |

the optimum. This also means there is no need to carry out expensive civil works to level the site of PV arrays, despite it being an extended custom in large PV plants.

The case of stand-alone systems designed to feed equipment having a constant consumption throughout the year is an especially interesting one, and deserves particular mention. The design criterion here is to maximise the energy captured during the period of least radiation, rather than throughout the year. As might be expected, such receivers are positioned perpendicular to the winter sunlight, which leads to recommend a tilt angle $\beta \approx \phi + 10^\circ$.

20.9.2 Sun-tracking Surfaces

At the moment, tracking mechanisms are little used in photovoltaics, but in the future they are likely to become much more common, mainly associated with relatively big grid-connected PV plants, where these mechanisms have already demonstrated very high reliability. As a particular example, the 100 kWp tracking system at the Toledo-PV plant [39] is in routine operation with 100% of availability from 1994 (about 66 000 h when writing this chapter).

Tracking about two axes maintains the receiver surface always perpendicular to the sun ($\beta = \theta_{ZS}$; $\alpha = \psi_S$). Hence, it allows collecting the maximum amount of energy possible. Mainly depending on the clearness index, the comparison with an optimally tilted fixed surface leads to the ratio $G_{dy}(2 \text{ axes})/G_{dy}(\beta_{opt})$ varying from 1.25 to 1.55 (column 4 divided by column 8 of Table 20.5). However, it is expensive to implement, because it uses relatively complicated mechanisms and takes up a great deal of space, due to the shadows cast. For these reasons, several types of one-axis trackers are usually preferred.

Azimuthal one-axis trackers rotate around their vertical axis, in such a way that the azimuth of the receiver PV surface is always the same as that of the sun's azimuth. Meanwhile, the tilt angle keeps constant ($\beta = \beta_{cons}$ and $\alpha = \psi_S$). The incidence angle is given by the difference between the surface's tilt angle and the solar zenith angle ($\theta_S = \theta_{ZS} - \beta_{cons}$). Obviously, the amount of collected radiation depends on the inclination of the surface, being the maximum for a value close to the latitude. Again, the sensitivity of the annual capture of energy to this inclination angle is relatively low. A typical value of approximately 0.4% loss from each degree of deviation from the optimum inclination can be assumed. Note that an azimuthal tracker tilted to the latitude collects up to 95% of the yearly irradiation corresponding to the case of two-axes tracking (column 5 divided by column 4 of Table 20.5).

One-axis trackers turning around a single axis-oriented N–S and tilted at an angle β_{NS} to the horizontal are also of great interest. It can be seen that, in order to minimise the solar incident angle, the rotation angle of the axis, $\psi_{NS} = 0$ at noon – must be

$$\tan \psi_{NS} = \frac{\sin \omega}{\cos \omega \cos \beta_{\Delta} - [\text{sign}(\phi)] \tan \delta \sin \beta_{\Delta}} \quad (20.54)$$

where $\beta_{\Delta} = \beta_{NS} - \text{abs}(\phi)$. The corresponding solar incident angle is given by

$$\cos \theta_S = \cos \psi_{NS} (\cos \delta \cos \omega \cos \beta_{\Delta} - [\text{sign}(\phi)] \sin \delta \sin \beta_{\Delta}) + \sin \psi_{NS} \cos \delta \sin \omega \quad (20.55)$$

A common configuration, called *polar tracking*, is when the axis is inclined just to the latitude. Then, the rotation axis is parallel to the rotation axis of the Earth, and the equations (20.54 and 20.55) become reduced to $\psi_{NS} = \omega$, and $\theta_S = \delta$. Because of the variation of the declination during the year, the cosines of the solar incident angle ranges between 0.92 and 1, having an annual mean value of about 0.95. This way, the polar tracker also collects about 95% of the energy corresponding to the two-axes case (column 7 divided by column 4 of Table 20.5). It is interesting to note that a polar tracker turns just at the same angular speed as that of a standard clock.

Another common configuration is when the axis is just horizontal. Horizontal one-axis trackers are of particularly simple construction and do not cast shadows in the N–S direction. This encompasses significant radiation reduction when compared with two-axis tracking (column 6 divided by column 4 of Table 20.5), but still significant radiation increase when compared with optimally tilted fixed surfaces (column 6 divided by column 8 of Table 20.5). Because of this, they are today the most common tracking solution in large PV plants: PVUSA [45], Toledo [39] and so on. And the same is true for solar thermal plants. We should remember that the very first solar tracker used in any significant way for power generation was just a N–S-oriented horizontal one-axis tracker associated to a parabolic reflecting trough, constructed in 1912 by Frank Shumann and C.V. Boys to power a 45-kW steam-pumping plant in Meadi, Egypt [46]. The tracking surface covered an area of 1200 m². The plant was a technical success, that is, reliable trackers existed already at the time, but it was shut down in 1915 due to the onset of World War I and cheaper fuel prices. The world's largest solar plant, at the well-known Luz solar field, erected in California from 1984 to 1986, also employs this type of tracking and, again, with great technical success [47]. The surface position and the solar incident angle are given by

$$\beta = \arctan \left| \frac{\sin \psi_S}{\tan \gamma_S} \right| \quad (20.56)$$

and

$$\cos \theta_S = \cos \delta \cdot [\sin^2 \omega + (\cos \phi \cos \omega + \tan \delta \sin \phi)^2]^{1/2} \quad (20.57)$$

Finally, it is worth commenting that large PV generators have several rows of modules mounted above the ground. The distance between rows affects the energy produced by the PV generator. If the separation is increased, fewer shadows are cast by some rows on the others and more energy is produced. But it also affects the cost, as greater separations lead to more land being occupied, longer cables and more expensive civil works. Therefore, there is an optimum separation, giving the best trade-off between greater energy and lower cost. There is a widely held view that tracking generally requires much more land than static arrangements. However, it should be outlined that this is not necessarily the case when horizontal one-axis tracking is concerned. The interested reader is encouraged to refer to [48], which deals in detail with tracking and shadowing in large PV arrays.

20.9.3 Concentrators

PV concentrators are able to capture only direct-beam solar radiation and require tracking mechanisms to keep in focus the solar cells. Therefore, they are best suited to sunny

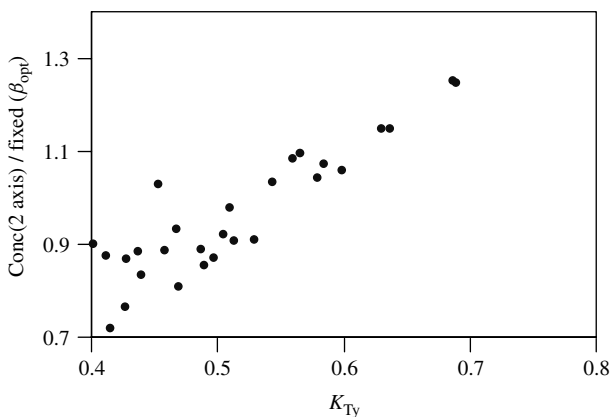


Figure 20.21 Comparison of annual average solar radiation available for fixed flat-plate conventional PV modules, and two-axis tracking PV concentrators. The y-axis is (column 10)/(column 9) and the x-axis column 4 of Table 20.5

sites with low scattering (or low diffuse radiation) and good solar resources. Figure 20.21 compares the amount of normal direct radiation for a PV concentrator mounted on a two-axis tracker, with the amount of global radiation, collected by a conventional flat-plate PV collector, at a fixed optimal tilt. The data represents the 30 locations in Table 20.5. The ratio between both quantities, $B_{dy}(\perp)/G_{dy}(\beta_{opt})$, (column 9 divided by column 8 of Table 20.5) is plotted against the annual clearness index. As a general rule, two-axis tracking concentrators collect more radiation than fixed flat-plate modules in places where $K_{Ty} > 0.55$.

20.10 PV GENERATOR BEHAVIOUR UNDER REAL OPERATION CONDITIONS

A problem that the engineer frequently has to solve is the prediction of the electrical behaviour of a PV generator, given the information about the generator's construction, geographic location, and the local weather. In particular, this represents the base for predicting the generator energy delivery, which is a critical step of any PV-system design. This leads to the question of establishing a PV module rating condition, at which power performance and other characteristics are specified and, defining a method for calculating performance at the prevailing environmental conditions such as solar irradiance, ambient temperature, wind speed and so on.

Traditionally, PV modules are being rated under the so-called Standard Test Conditions (STC) (Irradiance: 1000 W/m^2 ; Spectrum: $AM\ 1.5$; and Cell Temperature: 25°C). In the following, we will use the superscript $*$ to refer to these conditions. The most usual case is to know just the values of the short-circuit current, I_{SC}^* , the open-circuit voltage, V_{OC}^* and the maximum power, P_M^* , which are always included in the manufacturer's data sheets. Furthermore, the characterisation of the PV module is completed by measuring the *nominal operating cell temperature (NOCT)*, defined as the temperature reached by the cells when the PV module is submitted to an irradiance of 800 W/m^2 and

an ambient temperature of 20°C. However, performance predictions based on STC are being continuously questioned, mainly because the resulting annual energy efficiencies are significantly lower than the power efficiencies defined, using STC. Certainly, PV users can be astonished on learning that the real efficiency of the PV module they have purchased, once installed at home, has only about 70% of the STC efficiency they have read in the manufacturer's information. This could lead to a feeling of having been deceived. This frustration can even increase in the case of fraud, that is, if the actual STC power performance of the delivered PV module is below the value declared by the module's manufacturer, which, unfortunately, has sometimes been the case [49, 50].

All together, these facts have stimulated several authors to propose other methods for PV module rating and energy performance estimation, more oriented to give buyers clear and more accurate information about the energy generation of PV modules (see Chapter 16 for a detailed description on rating module performance). This is still an open question, and it is difficult to predict the extent to which these new models would be incorporated in future PV engineering practices. Most of these methods require extending testing to other-than-STC, and rely on a relatively large number of parameters that should be empirically determined. Surely, the use of a large number of parameters would potentially allow for more accurate energy modelling. But it is not clear as to what extent the possible improvements would compensate for the associated increase of complexity derived from the experimental determination of such parameters. The proponents of new methods tend to argue that their procedures can be easily implemented. (Their papers used to include sentences like ... *the entire test procedure for outdoor measurements, including the set-up, takes approximately three hours* ... [51]). But, at the same time, the PV module manufacturers are very reluctant to incorporate troublesome novelties into their module characterisation procedures already established at factory PV. This dilemma is, in fact, easily understandable considering the inherent difficulties associated with the adoption of any innovation. This was magnificently explained by Maquiavelo in his famous work *The Prince*, written in 1513: (... *There is nothing more difficult to plan, more doubtful of success ... than the creation of a new order of things* ...).

Together, claims of low PV modules energy performance, and the flourishing of proposals for new rating methodologies have led, no doubt, to significant confusion in today's PV community, making risky this author's task of selecting a particular methodology for recommending to his PV colleagues. However, it is this author's opinion that, at least in the case of crystalline silicon, energy performance modelling based on only a few parameters obtained at STC, and always included in the manufacturer's data sheets, can lead to adequate predictions, providing that some judicious considerations are made. Obviously, precautions to assure that actual STC power of the purchased PV modules correspond with the manufacturer's declarations are a different matter [52].

It must be remembered that crystalline silicon solar cells remain the workhorse for PV power generation, despite significant advances in other PV devices. For example, c-Si technology increased its world market share [53], from 84.4% in 1999 to 86.4% in 2000. This predominance means that actual information concerning in-field c-Si PV modules performance is particularly consistent, which is not typically the case where other materials are concerned. Because of this, dealing with c-Si PV modules is, by far, the simplest and easiest case for PV designers. This is why, despite the above-mentioned confusion, the

author dares to detail here a rather simple methodology that allows the estimation of the $I-V$ curve of c-Si PV modules operating in any prevailing environmental condition, exclusively using as input the values of I_{SC}^* , V_{OC}^* and P_M^* . In principle, such methodology can be extended to other-than-c-Si materials, and additional comments to do this are also included in the text that follows. However, the reader should be advised that the much less available experience with these materials encompasses significant increase in uncertainty.

20.10.1 The Selected Methodology

In a previous chapter (see Chapter 3), it has been shown that the characteristic $I-V$ of a solar cell can be expressed with sufficient accuracy by

$$I = I_L - I_0 \left(\exp \frac{V + IR_S}{V_t} - 1 \right) - \frac{V + IR_S}{R_P} \quad (20.58)$$

where I_L , I_0 , R_S and R_P are the photo-generated current, the dark current, the series resistance and the parallel resistance, respectively. The voltage V_t equals mkT/e (we recall that for $m = 1$, $V_t \approx 25$ mV at 300 K). This expression gives an adequate representation of the intrinsic behaviour of a typical c-Si solar cell. Nonetheless, it cannot be used directly to obtain the required predictions, because some parameters, I_L and I_0 in particular, cannot be established from the usually available information, often restricted to the values of I_{SC}^* , V_{OC}^* , and P_M^* , which are always included on the manufacturers' data sheets.

This difficulty is effectively overcome when the following assumptions, which are generally valid for c-Si PV cells and modules, are made:

- The effect of parallel resistance is negligible.
- The photo-generated current and the short-circuit current are equal.
- $\exp((V + IR_S)/V_t) \gg 1$ under all working conditions.

This allows equation (20.58) to be written as

$$I = I_{SC} - I_0 \exp \left(\frac{V + IR_S}{V_t} \right) \quad (20.59)$$

which, with $I = 0$, leads to the following expression for the open-circuit voltage:

$$V_{OC} = V_t \ln \left(\frac{I_{SC}}{I_0} \right) \quad (20.60)$$

whence

$$I_0 = I_{SC} \exp \left(-\frac{V_{OC}}{V_t} \right) \quad (20.61)$$

Substituting equation (20.61) in (20.59), we arrive at

$$I = I_{SC} \left[1 - \exp \left(\frac{V - V_{OC} + IR_S}{V_t} \right) \right] \quad (20.62)$$

This is a very useful expression. As we shall see, the values of all the parameters on the right-hand side are easily obtained allowing immediate application of the expression. An inconsistency arises in the sense that $I(V = 0) \neq I_{SC}$. Nevertheless, in all solar cells of practical use, we find that $V_{OC} \gg IR_s \Rightarrow I(V = 0) \approx I_{SC}$, which therefore makes this objection irrelevant. The expression can be inconvenient to use in the sense that I is implicit (it appears on both sides of the equation), theoretically making it necessary to solve the equation iteratively. However, for voltages close to the maximum-power point, a reasonably accurate solution can be obtained with only one iteration by setting $I = 0.9 \times I_{SC}$ in the second term.

The calculation of the maximum power can, in principle, be carried out by considering that the power is given by the product $P = VI$. The values of I_M and V_M , defining the maximum-power operation point, can be obtained from the usual condition for a maximum, $dP/dV = 0$. However, the implicit nature of the resulting expression makes it very cumbersome to use. It would be better to look for a simpler method, based on the existing relationship between the fill factor and the open-circuit voltage. According to M.A. Green [54] an empirical expression describing this relation is

$$FF = \frac{V_M I_M}{V_{OC} I_{SC}} = \frac{P_M}{V_{OC} I_{SC}} = FF_0(1 - r_s) \quad (20.63)$$

where

$$FF_0 = \frac{v_{OC} - \ln(v_{OC} + 0.72)}{v_{OC} + 1} \quad (20.64)$$

and $v_{OC} = V_{OC}/V_t$ and $r_s = R_s/(V_{OC}/I_{SC})$ are defined as the normalised voltage and the normalised resistance, respectively. It is interesting to note that the series resistance at STC can be deduced from the manufacturer's data by the expression

$$R_s = \left(1 - \frac{FF}{FF_0}\right) \frac{V_{OC}}{I_{SC}} \quad (20.65)$$

The values of V_M and I_M are in turn given by [55]

$$\frac{V_M}{V_{OC}} = 1 - \frac{b}{v_{OC}} \ln a - r_s(1 - a^{-b}) \text{ and } \frac{I_M}{I_{SC}} = 1 - a^{-b} \quad (20.66)$$

where:

$$a = v_{OC} + 1 - 2v_{OC}r_s \text{ and } b = \frac{a}{1 + a} \quad (20.67)$$

This set of expressions is valid for $v_{OC} > 15$ and $r_s < 0.4$. The typical accuracy is better than 1%. Their application to a photovoltaic generator is immediate, if all their cells are supposed to be identical, and if the voltage drops in the conductors connecting the modules are negligible.

Now, for the prediction of the $I-V$ curve of a PV generator operating on arbitrary conditions of irradiance and temperature, a good balance between simplicity and exactness is obtained through the following additional assumptions.

- The short-circuit current of a solar cell depends exclusively and linearly on the irradiance. That is,

$$I_{SC}(G) = \frac{I_{SC}^*}{G^*} G_{eff} \quad (20.68)$$

where G_{eff} is the “effective” irradiance. This concept must take into consideration the optical effects related to solar angle of incidence, as described in Section 20.7. Effects, as described by equations (20.46–20.59), are as follows:

- The open-circuit voltage of a module depends exclusively on the temperature of the solar cells T_c . The voltage decreases linearly with increasing temperature. Hence,

$$V_{OC}(T_c) = V_{OC}^* + (T_c - T_c^*) \frac{dV_{OC}}{dT_c} \quad (20.69)$$

where the voltage temperature coefficient, dV_{OC}/dT_c is negative. The measurement of this parameter used to be included in PV modules characterisation standards [51, 56] and the corresponding value must, in principle, be also included on the manufacturer’s data sheets. For crystalline silicon cells, dV_{OC}/dT_c is typically -2.3 mV per $^{\circ}\text{C}$ and per cell.

- The series resistance is a property of the solar cells, unaffected by the operating conditions.
- The operating temperature of the solar cell above ambient is roughly proportional to the incident irradiance. That is,

$$T_c = T_a + C_t G_{eff} \quad (20.70)$$

where the constant C_t has the value:

$$C_t = \frac{NOCT(^{\circ}\text{C}) - 20}{800 \text{ W/m}^2} \quad (20.71)$$

The values of $NOCT$ for modules currently on the market varies from about 42 to 46°C , implying a value of C_t between 0.027 and $0.032^{\circ}\text{C}/(\text{W/m}^2)$. When $NOCT$ is unknown, it is reasonable to approximate $C_t = 0.030^{\circ}\text{C}/(\text{W/m}^2)$. This $NOCT$ value corresponds to mounting schemes allowing the free air convection in both sides of the PV modules, which cannot be the case on roof-mounting arrays, that restrict some of the airflow. Then, it has been shown [57] that the $NOCT$ increases by about 17°C if some kind of back ventilation is still allowed and up to 35°C if the modules are mounted directly on a highly insulated roof.

Example: To illustrate the use and the usefulness of the equations of the above sections, we shall analyse the electrical behaviour of a PV generator rated at 1780 W (STC), made up of 40 modules, arranged 10 in series \times 4 in parallel. The conditions of operation are $G_{eff} = 700 \text{ Wm}^{-2}$ and $T_a = 34^{\circ}\text{C}$. It is known that the modules have the following characteristics under STC: $I_{SC}^* = 3$ A, $V_{OC}^* = 19.8$ V and $P_M^* = 44.5$ W. Further, it is known that each module consists of 33 cells connected in series and that $NOCT = 43^{\circ}\text{C}$.

The calculations consist of the following steps:

1. *Determination of the characteristic parameters of the cells that make up the generator under STC (equations 20.63–20.67):*

33 cells in series \Rightarrow Per cell: $I_{SC}^* = 3$ A, $V_{OC}^* = 0.6$ V and $P_M^* = 1.35$ W
 Assuming $m = 1$; $V_t(V) = 0.025 \times (273 + 25)/300 = 0.0248$ V $\Rightarrow v_{OC} = 0.6/0.0248 = 24.19 > 15$

Then, $FF_0 = (24.19 - \ln(24.91))/25.19 = 0.833$; $FF = 1.35/(0.6 \times 3) = 0.75$

And $r_s = 1 - 0.75/0.833 = 0.0996 < 0.4 \Rightarrow R_s = 0.0996 \times 0.6/3 = 19.93$ m Ω

$$a = 20.371; b = 0.953 \Rightarrow V_M/V_{OC} = 0.787 \text{ and } I_M/I_{SC} = 0.943$$

It is worth noting that these values lead to a value of $FF = 0.742$, slightly different from the starting value. This error shows the precision available by the method, better than 1% in this instance. Sometimes values of $m = 1.2$ or 1.3 give a better approximation.

2. *Determination of the temperature of the cells under the considered operating conditions (equations 20.70 and 20.71):*

$$C_t = 23/800 = 0.0287^\circ\text{C m}^2/\text{W} \Rightarrow T_c = 34 + 0.0287 \times 700 = 54.12^\circ\text{C}$$

3. *Determination of the characteristic parameters of the cells under the operating conditions being considered (equations 20.68 and 20.69):*

$$I_{SC}(700 \text{ W/m}^2) = 3 \times (700/1000) = 2.1 \text{ A}$$

$$V_{OC}(54.12^\circ\text{C}) = 0.6 - 0.0023 \times (54.12 - 25) = 0.533 \text{ V}$$

With R_s considered constant, these values lead to:

$$V_t = 27.26 \text{ mV}; v_{OC} = 19.55; r_s = 0.0785; FF_0 = 0.805; FF = 0.742; P_M = 0.83 \text{ W}$$

4. *Determination of the characteristic curve of the generator, (I_G , V_G):*

Number of cells in series 330; Number of cells in parallel: 4. Then:

$$I_{SCG} = 4 \times 2.1 \text{ A} = 8.4 \text{ A}; \quad V_{OCG} = 330 \times 0.533 \text{ V} = 175.89 \text{ V}; \quad R_{SG} = 1.644 \Omega; \\ P_{MG}^* = 1095.6 \text{ W}$$

$$I_G(A) = 8.4 \left[1 - \exp \frac{V_G(V) - 175.89 + 1.644 \cdot I_G(A)}{9.00} \right]$$

To calculate the value of the current corresponding to a given voltage, we may solve this equation iteratively, substituting I_G for $0.9 I_{SCG}$ on the first step. Only one iteration is required for $V_G \leq 0.8 V_{OCG}$. By way of example, the reader is encouraged to do it for $V_G = 140$ V and $V_G = 150$ V. The solution is $I_G(140 \text{ V}) = 7.77$ A and $I_G(150 \text{ V}) = 6.77$ A.

5. *Determination of the maximum power point:*

$$a = 17.48; b = 0.9458; V_M/V_{OC} = 0.7883; I_M/I_{SC} = 0.9332$$

$$V_M = 138.65 \text{ V}; I_M = 7.84 \text{ A}, P_M = 1087 \text{ W}.$$

Note that the ratio $P_M/P_M^* = 0.661$, while the ratio $G_{\text{eff}}/G^* = 0.7$. This indicates a decrease in efficiency at the new conditions compared to STC, primarily due to the greater solar cell temperature, $T_c < T_c^*$. An efficiency temperature coefficient can now be

obtained by

$$\frac{1}{\eta^*} \cdot \frac{d\eta}{dT_c} = \left(\frac{P_M}{P_M^*} \cdot \frac{G^*}{G_{\text{eff}}} - 1 \right) \cdot \left(\frac{1}{T_c - T_c^*} \right) = -0.004/^{\circ}\text{C}$$

This means the efficiency decrease is about 0.4% per degree of temperature increase, which can be considered as representative for c-Si.

It should be noted that, depending on the input data availability, other PV- generator modelling possibilities exist. For example, commonly I_M^* and V_M^* are given in the specifications in addition to their product P_M^* . Then, the series resistance can directly be estimated from equation (20.62). This leads to

$$R_S^* = \frac{V_{OC}^* - V_M^* + V_t \ln \left(1 - \frac{I_M^*}{I_{SC}^*} \right)}{I_M^*} \quad (20.72)$$

20.10.2 Second-order Effects

The model presented in the previous section is based only on standard and widely available information, which is an undeniable advantage, in particular for PV-system design. Furthermore, it is simple to use. However, it can be argued that such simplicity is at the price of neglecting the following:

- The effects of the parallel resistance
- The influence of the cell temperature in the short-circuit current.
- The influence of the irradiance in the open-circuit voltage.
- The non-linearity due to low irradiance.
- The spectral effects.
- The effects of wind.

It should be recognised that differences between expected and real energies delivered by PV modules are often mentioned in the literature [58]. Hence, it is worth reviewing the importance of each one of these previously neglected factors, with the aim of clarifying possible error sources. Many of these factors are discussed further in Chapter 16.

The influence of the parallel resistance is, to a great extent, compensated here, by the particular way of estimating the series resistance of a PV module, which assures that the maximum power of the modelled curve coincides exactly with that corresponding to the real one. Because of this, the accuracy of the model tends to be very good just around the maximum-power operation point, that is, just on the voltage region of interest.

The short-circuit current tends to increase slightly with increasing temperature. This can be attributed, in part, to increased light absorption, since semiconductor band gaps generally decrease with temperature, and, in part, to increased diffusion lengths of the

minority carriers. This can be considered by adding a linear term to equation (20.68). Thus

$$I_{SC}(G, T_c) = I_{SC}^* \cdot \frac{G}{G^*} \cdot \left[1 + (T_c - T_c^*) \frac{dI_{SC}}{dT_c} \right] \quad (20.73)$$

where the temperature coefficient dI_{SC}/dT_c depends on the semiconductor type and on the manufacturing process, but it is always quite small. Typical experimental values are below $3 \cdot 10^{-4}$ (A/A)/°C [51, 59]. For a solar cell operating at 70°C, that represents only 0.13% of I_{SC} increase. Hence, ignoring this dependence has no practical effects, in all the cases.

The open-circuit voltage tends to increase with the illumination level. The ideal diode equation (see equation (20.60)) shows there is a logarithmic dependence. Then, this effect can be considered by adding a logarithmic term to equation (20.69). Thus

$$V_{OC}(T_c, G) = V_{OC}^* + (T_c - T_c^*) \frac{dV_{OC}}{dT_c} + V_t \cdot \ln \left(\frac{G_{eff}}{G^*} \right) \quad (20.74)$$

Note that the relative influence of this new term increases with decreasing irradiance. For example, for $G_{eff} = 500$ W/m² and $G_{eff} = 200$ W/m², it represents about 3 and 7%, respectively. Hence, its importance when predicting the energy delivered by PV modules depends on the irradiance distribution of the irradiation content. Obviously, it is more important for northern than for southern countries. For example, in Freiburg-Germany ($\phi = 48^\circ$) about 50% of yearly irradiation is collected below 600 W/m² and 18% below 200 W/m². Meanwhile in Jaen-Spain ($\phi = 37.8^\circ$) about 30% of yearly irradiation is collected below 600 W/m² and only 6% below 200 W/m². Moreover, it should be understood that very low irradiances are sometimes rejected by PV-system requirements. For example, in grid-connected systems, DC power from PV modules must be large enough to compensate for the inverter losses. Otherwise, the PV system becomes a net energy consumer.

While this logarithmic term does account for some variation in open-circuit voltage as irradiance changes, it does not adequately predict the rapid decrease observed at values of irradiance less than about 200 W/m², which causes a noticeable efficiency decrease below this value. The use of a second logarithmic term has been proposed [60] to also consider this low irradiance effect. Thus

$$V_{OC}(T_c, G) = \left[V_{OC}^* + \frac{dV_{OC}}{dT_c} (T_c - T_c^*) \right] \left[1 + \rho_{OC} \ln \left(\frac{G_{eff}}{G_{OC}} \right) \ln \left(\frac{G_{eff}}{G^*} \right) \right] \quad (20.75)$$

where ρ_{OC} and G_{OC} are empirically adjusted parameters. Values of $\rho_{OC} = -0.04$ and $G_{OC} = G^*$ have proven adequate for many silicon PV modules.

The sun spectrum shifts over time, due to changes in atmosphere composition, and changes in the distance the light has to travel through the atmosphere. This can affect the response of PV devices, especially if they have a narrow spectral response. Martin and Ruiz have proposed [61] a model based on the parameterisation of the atmosphere by means of the clearness index and the air mass, and this considers independently the spectrum of each radiation component: direct, diffuse and albedo. It can be described by

modifying the equation (20.68). Thus

$$I_{SC} = \frac{I_{SC}^*}{G^*} (B_{eff} \cdot f_B + D_{eff} \cdot f_D + R_{eff} \cdot f_R) \quad (20.76)$$

where f_B , f_D and f_R obeys to the general form

$$f = c \cdot \exp[a(K_T - 0.74) + b(AM - 1.5)] \quad (20.77)$$

and a , b and c are empirically adjusted factors, for each module type and for each radiation component. Note that 0.74 and 1.5 are just the values of the atmospheric parameters corresponding to the STC. Table 20.7 shows the recommended values of these parameters for crystalline, c-Si, and amorphous a-Si modules. The usefulness of this table can be extended to other PV materials, by linear interpolation on the energy band gap, E_g , between $E_g(\text{c-Si}) = 1.12 \text{ eV}$ and $E_g(\text{a-Si}) = 1.7 \text{ eV}$. For example, $E_g(\text{a-SiGe}) = 1.4 \text{ eV} \Rightarrow$ estimated value of c is equal to 0.8.

Spectral effects used to be small on a yearly basis. Spectral losses with respect to STC are typically below 2% with semiconductors with broad spectral sensitivity, and below 4% for the others. However, on an hourly basis, spectral effects up to 8% can be encountered.

The PV module cell temperature is a function of the physical variables of the PV cell material, the module and its configuration, the surrounding environment and the weather conditions. It results from the balance of energy inputs and outputs through radiation, convection, conduction and power generation. Today, the more widely extended model, based on the *NOCT* concept and described by equations (20.70 and 20.71), lump the contributions together in an overall heat-loss coefficient, resulting in a liner relationship between module temperature and irradiance under steady-state conditions. This implies accepting that the heat transfer process between the solar cell and the ambience is essentially dominated by the conduction through the encapsulating materials, and neglecting the wind effects on convection. This model is simple to use and requires only standard available input information, which are undeniable advantages for the PV designer. But it can lead to significant errors in cell temperature estimation for non-steady-state conditions [62] (observed thermal time constant of PV modules is about 7 minutes), and for high wind speeds. That has stimulated several authors to develop new thermal models for PV systems, based not only on irradiance but also on wind speed. For example, Sandia

Table 20.7 Coefficient for spectral response modelling, for c-Si and a-Si modules

| | B | | D | | R | |
|-----|-----------|-----------|-----------|-----------|-----------|-----------|
| | c-Si | a-Si | c-Si | a-Si | c-Si | a-Si |
| c | 1.029 | 1.024 | 0.764 | 0.840 | 0.970 | 0.989 |
| a | -3.13E-01 | -2.22E-01 | -8.82E-01 | -7.28E-01 | -2.44E-01 | -2.19E-01 |
| b | 5.24E-03 | 9.20E-03 | -2.04E-02 | -1.83E-02 | 1.29E-02 | 1.79E-02 |

Table 20.8 Temperature coefficients for module and cell temperature estimation, for two typical module designs

| Type | T_1 [°C] | T_2 [°C] | b | ΔT [°C] |
|-------------------|---------------|---------------|--------|--------------------|
| Glass/cell/glass | 25.0 | 8.2 | -0.112 | 2 |
| Glass/cell/teflar | 19.6 | 11.6 | -0.223 | 3 |

Laboratories proposed [63] a two components thermal model given by

$$T_c = T_m + \frac{G_{\text{eff}}}{G^*} \Delta T, \text{ where } T_m = T_a + \frac{G_{\text{eff}}}{G^*} [T_1 \exp(b \cdot \omega_s) + T_2] \quad (20.78)$$

In this equation, T_m is the back-surface module temperature, in °C; ω_s is the wind speed measured at standard 10 m height, in m.s^{-1} ; T_1 is an empirical coefficient determining the upper temperature limit at low wind speeds; T_2 is an empirical coefficient determining the lower temperature limit at high wind speeds; b is an empirical coefficient determining the rate at which the module temperature drops as wind speed increases and ΔT is also an empirical coefficient related to the temperature gap along the back encapsulation material. Table 20.8 gives the parameters found to have good agreement with measured temperatures, for two different module types.

However, the real usefulness of all these second-order corrections (equations 20.74–20.77) for temperature and wind speed is far from clear, because wind speed is difficult to predict, and also because cell temperature errors becomes more tolerable when translated into PV module power generation. For example, for a solar cell operating around 50°C, an error of 20% on the estimation of its cell temperature ($\approx 10^\circ\text{C}$) reflects in an error of only 0.4% ($\approx 10^\circ\text{C} \times 2.3(\text{mV}/^\circ\text{C})/600 \text{ mV}$) in the estimation of the corresponding power.

20.11 RELIABILITY AND SIZING OF STAND-ALONE PV SYSTEMS

The merit of a stand-alone PV system depends on how reliably it supplies electricity to the load. It is customary to quantify this reliability in terms of the Loss of Load Probability (*LLP*), defined as the ratio between the energy deficit and the energy demand, both referring to the load, over the total operation time of the installation. Thus,

$$LLP = \frac{\int_t \text{energy deficit}}{\int_t \text{energy demand}} \quad (20.79)$$

It should be noted that, because of the random nature of solar radiation, the value of *LLP* is always greater than zero, even if the PV system never actually breaks down. The available literature shows a large consensus over the expression of reliability in terms

of energy shortage probability, but different names can be found for the *LLP*: Deficit of Energy [64], Loss of Power Probability [65] and Loss of Power Supply Probability [66]. Moreover, the Load Coverage Rate [67] or Solar Fraction [68], *SF*, defined as the fraction of energy load covered by the PV system is also used to quantify reliability. Clearly, $SF = 1 - LLP$.

The “size” of a PV system means the size of both the generator (PV modules) and the accumulator (batteries or other storage device). It is useful to relate these sizes to the size of the load, in terms of average daily energies. Thus, the generator capacity, C_A , is defined as the ratio of the average daily energy output of the generator divided by the average daily energy consumption of the load. The accumulator capacity, C_S , is defined as the maximum energy that can be extracted from the accumulator divided by the average daily energy consumption of the load. Thus,

$$C_A = \frac{\eta_G \cdot A_G \cdot \overline{G_d}}{L} \text{ and } C_S = \frac{C_u}{L} \quad (20.80)$$

where A_G and η_G are the area and conversion efficiency of the photovoltaic generator, respectively, $\overline{G_d}$ is the mean value of the daily irradiation on the surface of the generator, L is the mean value of the daily energy consumed by the load and C_u is the useful energy storage capacity of the accumulator. More strictly, η_G should be the path efficiency from the array to the load, and C_u is the product of the nominal capacity (which refers to the whole energy that can be extracted from the accumulator if no particular limitations were imposed) and the maximum allowable depth of discharge. We will deal with the practical meaning of such parameters later. Meanwhile, it is worth pointing out that C_A depends on the local solar climate conditions. Therefore, the same photovoltaic generator, connected to the same load, may seem big in one place and small in another where there is less radiation.

Figure 20.22 shows how the energy generation varies over an assumed period of j days, for a given location and load, and for two different sizes of the generator ($C_{A1} < C_{A2}$). The shaded areas underneath the line $y = 1$, illustrate the temporal deficits of energy generation that need to be compensated by extraction of energy from the accumulator. It can be observed that the larger the generator, the lower the deficit and, hence, the smaller the required accumulator. Two ideas are now intuitively apparent: the first is that it is possible to find different combinations of C_A and C_S that lead to the same value of *LLP*; the second is that the larger the photovoltaic system, the better the reliability, that is, the lower the value of *LLP*, but also the greater the cost.

A certain degree of reliability is (or should be) a requirement depending on the typology of the load. For example, reliability requirements of telecommunication equipment are usually higher than that required by domestic appliances (higher reliability means lower *LLP* values). The problem confronting the PV engineer then takes the following “theoretical” form: Which combination of C_A and C_S achieves the desired *LLP* with minimum cost? Since cost estimation is a classic economic problem discussed widely in the literature, the PV-sizing problem is mainly rooted in the relationship between C_A , C_S and *LLP*. Later, C_A and C_S must be translated into the number and power of PV modules and battery capacity.

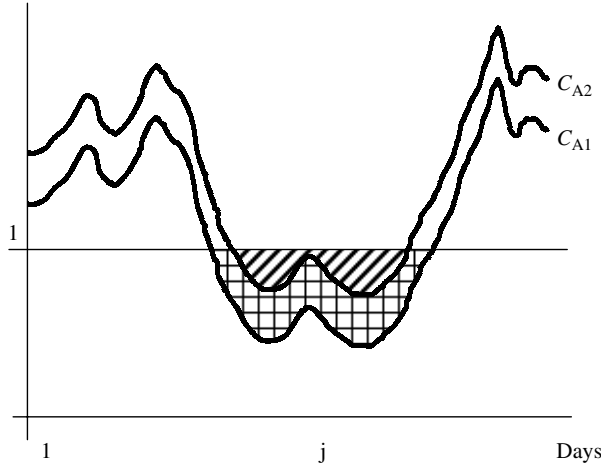


Figure 20.22 Time variation of the generated daily energy, relative to load, for two PV generators for which $C_{A1} < C_{A2}$. The shadowed areas represent the corresponding energy deficits to be covered by the storage device

In essence, any PV- sizing method involves four different steps:

- obtaining solar radiation site information,
- preparation of global horizontal daily irradiation sequences,
- transposition from horizontal to inclined radiation values,
- simulation of PVsystem behaviour, in order to quantify *LLP* corresponding to pairs of C_A and C_S values.

The first three steps have already been discussed in previous sections of this chapter. We will now deal with the last step, with the following assumptions: first, the daily energy consumption is constant all through the year; second, all the daily consumption occurs at night (i.e. after the energy generation time ends); and, third, the components of the PV system are ideal and can be linearly modelled. This is adequate for analysing the “pure” sizing problem, that is, the relation between C_A , C_S and *LLP*. Non-linearities and non-ideal effects (for example, battery efficiency) are better taken into account by the use of proper correction factors when translating C_A and C_S values into nominal PV array power and battery capacity. It is interesting to note that short-term (hourly) variations of demanded energy have no effect on *LLP* [64, 69], provided that $C_S > 2$, which is usually the case. The above- described assumption leads to particularly simple calculations. The state of charge, *SOC*, of the accumulator at sunset of day j is given by

$$SOC_j = \min \left\{ SOC_{j-1} + \frac{C_A \cdot G_{dj}}{C_S \cdot \bar{G}_d} - \frac{1}{C_S}; 1 \right\} \quad (20.81)$$

where G_{dj} is the total irradiation for day j , and

$$LLP = \frac{\sum_{j=1}^N E_{LACK,j}}{N \cdot L} \quad (20.82)$$

where N is the number of days for which the simulation is carried out, and E_{LACK} is the daily energy deficit, given by

$$E_{\text{LACK}j} = \max \left\{ \frac{1}{C_S} - \text{SOC}_j; 0 \right\} \quad (20.83)$$

This equation implies that an energy deficit occurs only when the stored energy at the end of the day $\text{SOC}_j \cdot C_S \cdot L$ does not suffice to cover the daily load L . Note that $\text{SOC}_j \cdot C_S \cdot L < L \Rightarrow (1/C_S - \text{SOC}_j) > 0$.

Because information on the daily irradiation used to be expressed in terms of mean monthly values, a different value of C_A may be worked out for each month. In what follows, we shall use for C_A just the value corresponding to the worst month. Thus,

$$\overline{G_d} = \min\{G_{dm}(\beta, \alpha)\}; (m = 1, \dots, 12) \quad (20.84)$$

Computed results can be arranged and presented graphically. Figure 20.23 presents some examples of the so-called “reliability maps”.

The shape of such curves prompts the thought that it should be possible to describe them in an analytical form. Several attempts at proposing analytical methods based on this idea have been made [64, 70–76] allowing sizing of PV systems by means of straightforward, simple calculations. For example, at the IES-UPM we have concluded [76] that all these curves conform to the relationship

$$C_A = f \cdot C_S^{-u} \quad (20.85)$$

where f and u are two parameters that depend on the value of LLP and on the location. These parameters do not have particular physical meaning, and their determination previously requires a lot of simulations to be carried out. However, they allow a large number of simulated results to be condensed into just a few sizing parameters. Advanced simulation software tools have also been developed and are being marketed today [42, 43].

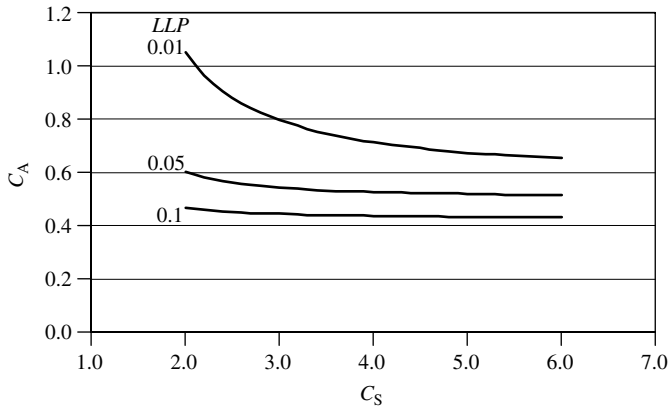


Figure 20.23 Reliability maps: Generator capacity C_A versus storage capacity C_S with the reliability LLP as parameter

It must be stressed that, whatever the detailed methodology, PV-system sizing relies on future prediction (the expected system lifetime) based on past observations of the solar radiation. Basic statistical laws imply that such prediction exercises are unavoidably associated with a degree of uncertainty, as mentioned before. This implies a basic limit of accuracy for PV sizing. We will try to clarify this aspect with an example.

We will suppose that 20 years of daily irradiation data measured in a certain location with a great level of accuracy are available. We will call them the “historical sequence”. This allows us first, to establish the statistical characteristics of the radiation (mean value, standard deviation, etc.); and, second, to make detailed simulations of a PV system’s behaviour over these particular years. Thus, we can map with high precision the reliability associated with different system sizes, for this particular historical sequence. As a simulation exercise, the accuracy of the result is limited only by the precision of the initial measurements, which have been assumed to be very good. However, when using such a sequence for sizing a future system, another limitation arises simply because the solar radiation in the future will not exactly repeat the same pattern as in the past. In fact, it is extremely unlikely in terms of daily sequences. All that can be expected is that the future solar radiation sequence will keep some statistical properties whose validity is known to be general, which opens the door for the generation of a vast collection of hypothetical solar radiation sequences with the same occurrence probability as the historical one. Then, a different reliability map can be associated with each of these radiation sequences, by means of the above-mentioned simulation exercise. Obviously, the similarity between the different maps can be understood as a measure of the uncertainty associated with the prediction. Figure 20.24 shows the result of superimposing such maps. The example is for Madrid, generating different solar radiation sequences following the above-mentioned Aguiar’s method [37]. It is clear that precautions must be taken with predictions for $LLP < 10^{-2}$. For example, for $LLP = 10^{-3}$ and $C_S = 3$, we can find C_A values from 1.1 to 1.5. Other authors [70, 77] have presented similar results. We must conclude that the validity of PV-sizing methodologies is generally restricted to the range $1 > LLP > 10^{-2}$, that is, to solar coverage below 99%. Beyond this limit, sizing results are statistically of doubtful quality, although unfortunately, they are often found in the literature and in simulation software tools marketed today.

It must be stressed that this basic uncertainty cannot be overcome either by reducing the simulation time-step (hourly instead of daily values) or by incorporating more complex models of the elements of the PV systems (non-linear $I-V$ models of PV generators, battery efficiency dependence with SOC etc.). In fact, the reduction of the considered simulation period can only worsen the situation. It can be shown that the validity of sizing results based only on the TMY (avoiding the generation of large-radiation sequences) is restricted to the range $1 > LLP > 10^{-1}$, independent of any other consideration [78]. Appropriately, Marion and Urban [18], when presenting USA TMY s, advises “... *Because they represent typical rather than extreme conditions, they are not suited for designing systems to meet the worst-case conditions occurring at a location*”.

On the other hand, such basic uncertainty can help to explain why the result of the different PV-sizing methods can be inconsistent; and also why the accuracy gains associated with the consideration of second-order effects when modelling the PV system are likely to be insignificant. In other words, such modelling can be useful for studying some PV-system features (optimal number of solar cell per module, optimal charge regulation

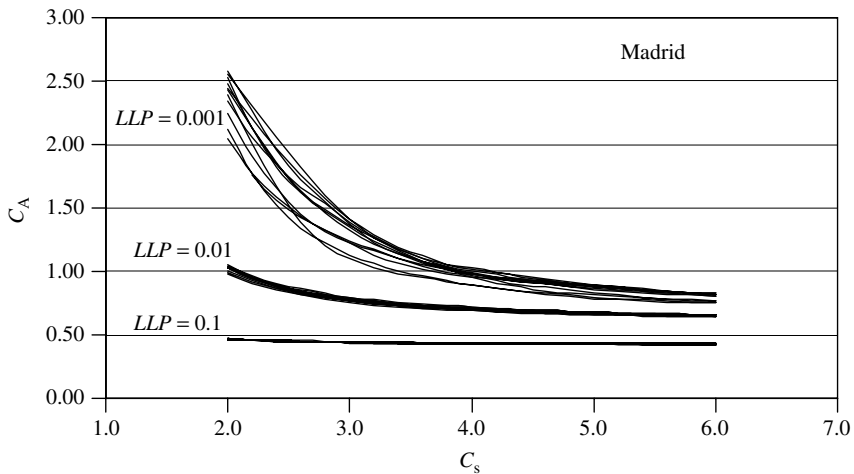


Figure 20.24 Simulated reliability maps, C_A versus C_S , with the historical and with 12 generated solar radiation sequences for three different reliability LLP values

algorithms etc.); but it is of little value when considering the pure size problem, for which a judicious and rather simple hypothesis suffices. A similar conclusion is presented in Kaiser and Sauer [79], from a comparison of the long-term energy yield of stand-alone PV systems simulated with both simple and detailed models. The authors observe that the range of uncertainty due to possible fluctuations of the radiation-time series is significantly larger than the those corresponding to changes in the PV-system component modelling, and conclude “*The results make it clear that exact simulation models can provide exact numbers, but do not automatically allow exact predictions*”.

This can also help explain why PV-system sizing simply based on guesswork remains widely practiced in current engineering practices. This prevents any quantitative relationships between C_A , C_S and LLP being established. The size of the generator is instead chosen to ensure that the energy produced during the design period (most often, the worst month) exceeds the demand of the load by a margin that depends on the designer’s experience. A similar procedure is used to size the accumulator. In summary,

$$C_A = F_{S1} \text{ and } C_S = F_{S2} \quad (20.86)$$

where F_{S1} and F_{S2} are arbitrary factors. For example, $C_A = 1.1$ and $3 \leq C_S \leq 5$ are common values for rural electrification purposes [80]. $1.2 \leq C_A \leq 1.3$ and $5 \leq C_S \leq 8$ are common ranges on the so-called professional market [71]: telecommunication and so on.

It is worth pointing out that this rather unscientific way of proceeding does not necessarily give bad results, in terms of reliability and cost. As a matter of fact, a proper combination of expertise and common sense often leads to very good results. Today, PV systems have the reputation of being reliable, even in those sectors where high reliability is an established requirement, such as telecommunications and cathodic protection. This helps explain why reliability quantification is generally considered irrelevant in real

engineering practice, and mainly good for academic discussion; and why the actual use of PV-sizing methodologies is mainly aimed at giving a pseudo-scientific appearance to commercial activities. Our own experiences at IES-UPM contain several cases of perplexed PV clients requesting our opinion on the big PV-system sizing differences among different PV contractor estimates that they have received for a given location and application. Obviously, simplistic relations like equation (20.86) do not help the PV professional to adopt rigorous sizing procedures. However, we still believe such rigorous procedures should play an important role in future. This is because a professional's credibility benefits from reliability quantification (the use of the Mean Time Between Failures concept in the conventional electricity sector is a good example of this); and also because the usefulness of such methods extends beyond pure sizing problems. Additional comments are given in the following section.

It must be mentioned that in the common case of PV arrays directly coupled to batteries, that is without maximum power-tracking devices, energy balance analysis can be done by means of simple ampere balances, initially supposing that the working voltage is always the nominal one, V_{NOM} , at which it equals the maximum power point voltage of the generator. Therefore,

$$L = V_{\text{NOM}} \cdot Q_L \text{ and } \eta_G \cdot A_G = \frac{V_{\text{NOM}} \cdot I_M^*}{G^*} \quad (20.87)$$

which leads to

$$C_A = \frac{I_M^* \cdot G_{\text{dm}}(\beta, \alpha)}{Q_L \cdot G^*} \text{ and } C_S = \frac{Q_B}{Q_L} \quad (20.88)$$

where Q_L is the amount of charge (expressed in ampere-hours) drawn daily by the load, that characterises the required PV array, and Q_B is the useful ampere-hour capacity of the battery, which is equal to the product of the nominal capacity by the maximum depth of discharge. This approximation, in spite of appearing oversimplified, gives very good results and simplifies the task of deducing the number of PV modules to be installed.

20.12 THE CASE OF SOLAR HOME SYSTEMS

Global market indicators [81, 82] lead to the estimate that about 1.3 million home systems for lighting, radio and television are currently in operation, totalling 40 MW_p, and large rural electrification programmes comprising some thousands of SHSs are increasingly becoming a part of the rural market. Thus, SHS represent the most widespread PV application nowadays, and the trend is likely to continue.

Standardisation of equipment and its mass production represent efficient ways to obtain low prices and high technical quality. In consequence, SHS designers have to fix a single “standard” value of energy consumption for a large number of different families. It must be noted that such standardisation is a requirement imposed by the technology itself in order to reduce cost and guarantee quality, but it does not correspond well with the idea of needs at the individual level. PV history shows some interesting cases [83, 84]. For example, in Reference [83] it is stated that “... *an interesting aspect,*

clearly confirmed by the operating results of ENEL plants, is that the intake power by this type of user . . . is rarely the same on any given day, and it is linked to the particular lifestyle of the people involved, to periods of absence and to the number of occupants of the houses being supplied, and so on". Apart from PV, other types of rural electrification also provide examples. Figure 20.25 shows the distribution of the individual monthly electricity consumption measured along four years in the 63 dwellings of Iferd, a Moroccan village where a small diesel generator set provides 3 h of electricity per day (consumers are metered and pay for their energy use). The large observed spread leads one to question the real meaning of reliability parameters such as *LLP*, and the real usefulness of rigorous PV-sizing methodologies.

It appears that "standard" *LLP* values derived from sizing methodologies are scarcely representative of the realities in the field. The relationship between reliability and load, that is, the function $LLP = LLP(L)$ for a given PV system, can be explored just by extending the previously described simulation procedure to a large number of cases. A certain baseline case has been, first, established by fixing the PV array power and the battery capacity values, C_A and C_S , for a given load, L_{BASE} , and a given reliability, $LLP = 0.1$. Then, the load has been varied from $0.8 L_{BASE}$ to $1.2 L_{BASE}$ and the corresponding reliability has been calculated. Figure 20.26 shows the result. Roughly speaking, we can say that an approximately logarithmic relationship exists in such a way that *LLP* decreases one order of magnitude for each 30% of load reduction. This result, together with the observation that real L values are generally found within the range -50% to $+100\%$ of the mean, let us conclude that real individual *LLP* values can vary more than three orders of magnitude (for example, from 10^{-1} to 10^{-4}) in the context of the same SHS project. This nullifies any attempt at finding a single representative

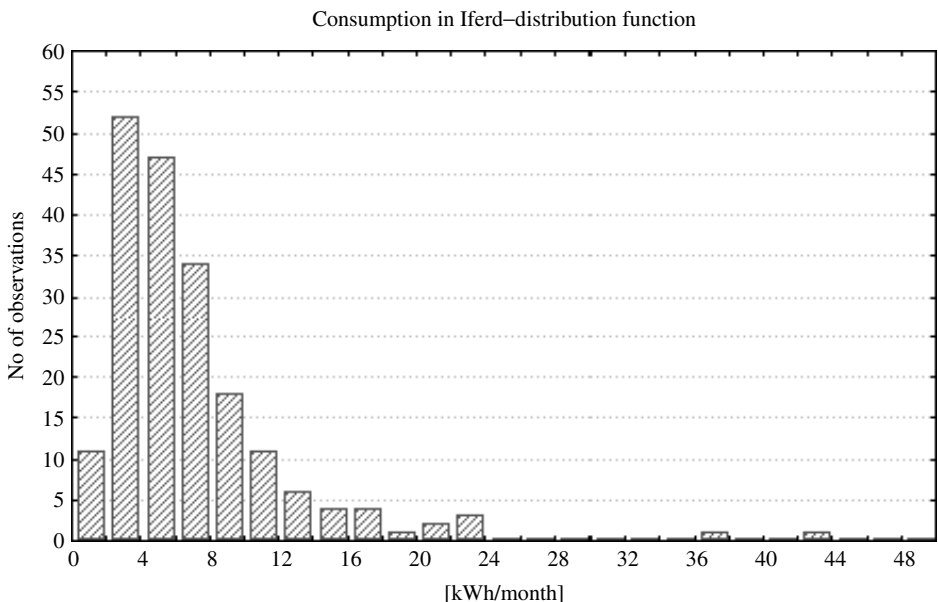


Figure 20.25 Distribution function of monthly electricity consumption in all the Iferd dwellings

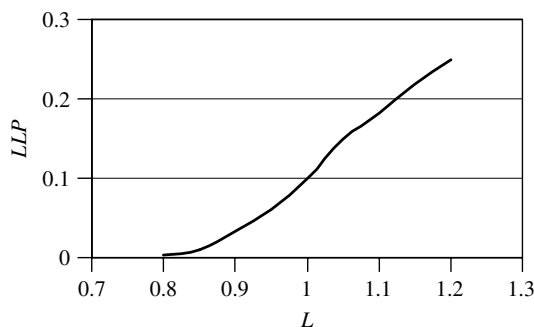


Figure 20.26 Reliability LLP as a dependent variable on the consumption L for a given PV array and capacity values

LLP value. It is worth mentioning that the same is not true when centralised electricity generators are considered (PV or not), because the total energy consumed by all the families involved shows a much lower standard deviation than that corresponding to the individual consumptions (roughly, the standard deviation becomes reduced by a factor of $1/\sqrt{N}$, N being the number of families), so that it is possible to find single L and LLP representative values for the whole served population.

However, even in extremely varying applications, such as SHS, PV-sizing methods based on reliability can be of great help if large-scale programmes become a future reality. This will probably require the development of rigorous engineering: standardisation of different levels of service, technical quality controls and so on. For example, PV-sizing methods based on LLP represent an interesting possibility of comparing different alternatives (different offers from various manufactures) on an objective basis, as the LLP value respectively associated to each alternative, for the same considered energy service [78].

It is worth considering the question: “How much electricity has to be provided to a rural house in a developing country to be socially and economically acceptable?” Although this question is always at the origin of any PV rural electrification programme, its answer in terms of watt/hour/day, is far from being clear. Energy consumption data, based on practical experience in developing countries, are scarce in the literature [84], which is paradoxical considering that many thousands of SHS are currently operating in developing countries. Instead, there are a great number of consumption scenarios where, although starting from very different hypothesis concerning the number of appliances and the length of time they are in use, the SHSs finally selected have an installed power of about 40 to 50 Wp. This is because past in-field experience has shown PV designers that such systems are generally well accepted by the rural users, while the same is not always the case when small (20–30 Wp) PV modules are concerned. This way, the SHS scenarios elaborated by PV designers must therefore be interpreted as explanation exercises, rather than as designs for systems starting from an evaluation of actual needs (see Chapter 23 for discussion of rural electrification programmes). So, we must conclude that energy scenarios for rural electrification purposes are still an open question, which need to be explored in-depth.

20.13 ENERGY YIELD OF GRID-CONNECTED PV SYSTEMS

The output of grid-connected PV systems is the output from the PV array less the losses in the inverter. The output from the PV array has been considered in detail in this chapter, and the performance of inverters is described in Chapter 19. As far as inverters are concerned, it is important to account for the fact that the instantaneous efficiency, η_y , depends on the ratio between the actual power delivered to the grid P_{AC} , and the rated power of the inverter, P_{IMAX} . This dependence may be represented by [85]

$$\eta_i = \frac{p}{p + k_0 + k_{i1}p + k_{i2}p^2} \quad (20.89)$$

where $p = P_{AC}/P_{IMAX}$ and k_0 , k_{i1} and k_{i2} are parameters characteristic of the inverter defining its electrical behaviour. k_0 is the quiescent power consumption, k_{i1} represents the losses that depend linearly on the current (voltage drop across diodes, etc.) and k_{i2} represents the losses that depend on the square of the current (resistive losses, etc.). These parameters can be obtained from the inverter efficiency curve. Depending on quality level, input voltage and rated power, the loss parameters of existing inverters have a spread of more than a factor of 10. Average values, in percentage, are $k_0 = 2$, $k_{i1} = 2.5$ and $k_{i2} = 8$, leading to 85% typical energy efficiency. Very good inverters reduce these values to $k_0 = 0.35$, $k_{i1} = 0.5$ and $k_{i2} = 1$, leading to 95% typical energy efficiency.

To describe the effect of no-load shut-off, the standby self-consumption k'_0 is used. It is the value to which the operating self-consumption (k_0) is reduced during shut-off ($k'_0 < k_0$). Reduction of self-consumption improves the low- and medium-power efficiency, which is most important for PV applications. The loss fractions due to self-consumption sum up to considerable losses in PV systems. In comparison, the sum of the load dependent losses (due to k_1 and k_2) is 1.5 to 7 times smaller.

Standard methods for performance analysis of PV grid-connected plants have been introduced in the JRC Ispra Guidelines [86] and extended and improved by HTA Burgdorf [87]. Global performance is appropriately described by the so-called *performance ratio* (PR), which is the ratio of AC energy delivered to the grid, E_{AC} , to the energy production of an ideal, loss-less PV plant with 25°C cell temperature and the same solar irradiation. This gives a good indication of how much of the ideally available PV energy has actually been used. It is given by

$$PR = \frac{E_{AC}}{\frac{G_y(\beta, \alpha)}{G^*} \cdot P_M^*} \quad (20.90)$$

Other interesting parameters are the *Reference Yield*, $Y_r = G_y(\beta, \alpha)/G^*$, the *Array Yield*, $Y_a = E_{DC}/P_M^*$, where E_{DC} is the DC energy generated by the PV array, and the *Final Yield*, $Y_f = E_{AC}/P_M^*$. All the three have units of time, and allow us to distinguish between the losses due to the PV array, and the losses associated to the inverter and to the operation of the system. Capture losses, $L_C = Y_r - Y_a$, are defined as the energy losses, expressed in hours per day of PV array operation at STC power output, caused by: cell temperatures

Table 20.9 Power distribution of the yearly irradiation for a low and a high latitude location

| Location | $G_y(\beta_{\text{opt}})$ [kWh/m ²] | Percent of irradiation in different ranges of irradiance in [W/m ²] | | | | |
|------------|--|---|---------|---------|------|-------|
| | | <200 | 200–500 | 500–800 | >800 | Total |
| Jaen | 2040 | 5.8 | 23.6 | 44.7 | 25.9 | 100 |
| Copenhagen | 1190 | 13.9 | 30.7 | 35.7 | 19.7 | 100 |

higher than 25°C, losses in wiring and protection diodes, poor module performance at low irradiance, partial shading, snow and ice coverage, module mismatch, operation of the array at a voltage other than its maximum power point, and spectral and angular losses. *System losses*, $L_S = Y_a - Y_f$, are the losses due to inverter inefficiencies. It must be noted that $PR = Y_f/Y_r$.

Energy losses in good PV grid-connected systems are about $L_C = 15\%$ and $L_S = 7\%$, which lead to $PR \approx 0.78$. However, reported experimental values have ranged from 0.65 to 0.72. The main reason for such PR reduction is that the actual power of installed PV arrays is often below the rated power declared by the manufactures [88].

The power distributions of solar irradiation are different for varied geographical latitudes. In places of high latitude, with very cloudy weather, the solar irradiation is almost evenly distributed over a wide range of power scale; while in low latitude places, with predominantly clear sky, the higher power range is enhanced. Table 20.9 presents the distribution in different irradiance classes of the total yearly irradiation over an optimally tilted surface, as obtained from the *TMY* of Copenhagen [89] ($\phi = 55.7^\circ$) and Jaen-Spain [90] ($\phi = 37.8^\circ$). Surprisingly, the energy content at low irradiances ($G < 200 \text{ W/m}^2$) is relatively low in both places. This may appear counter-intuitive, but it is easily understood when considering the difference between time and energy distribution. For example, in Copenhagen, the low irradiance (<200 W) accounts for only 13.9% of the total annual irradiation, despite it occurring during 2461 h/year, which represents 55% of the total daily time. That leads one to question the idea, sometimes defended in PV literature [91], that PV module performance at low irradiances is very relevant for cloudy climates. As a matter of fact, empirical evidence that efficiency at low light levels is scarcely relevant is found in the literature [92].

However, because the most commonly occurring irradiation corresponds to medium irradiances, an energetic advantage can be obtained by selecting the inverter size smaller than the PV generator peak power, that is, $P_{\text{IMAX}} < P_M^*$. The corresponding reduction of relative inverter self-consumption and losses may compensate the possible energy loss by an inverter power limit lower than the maximum PV output power. Recommended values of P_{IMAX}/P_M^* range from 0.6 (high latitudes) to 0.8 (low latitudes) [85, 93].

20.14 CONCLUSIONS

Methods to estimate all the solar radiation components incident on any arbitrarily oriented surface and at any time of the year have been presented. The only required input

information is the 12 monthly mean values of the daily global horizontal irradiation. Several sources of solar radiation data are available. The corresponding values, for the same location and the same month, can significantly differ from one source to another. The corresponding uncertainty does not derive primarily from a lack of precision in the measuring instruments, but from the random nature of the solar radiation. The intrinsic uncertainty of solar radiation represents an important limit to the significance of the results of any PV design exercise, irrespective of the complexity of the model supporting the particular design tool. Because of this, rather simple design methodologies can yield results of similar confidence that results from sophisticated ones. The annual solar radiation availability on horizontal surfaces, optimally tilted fixed surfaces and several types of tracking surfaces has been calculated for 30 different places distributed all over the world. The hope is that the readers could find here a similar location, both in latitude and clearness index, to the location of their interest.

On the other hand, the PV module's conversion efficiency of solar radiation into electricity has also been considered. A model for predicting the $I-V$ characteristic of a PV generator at any prevailing condition such as solar irradiance, ambient temperature, wind speed and so on, have been described. The only required input data are the short-circuit current, the open-circuit voltage and the maximum power under the STC, and the Nominal Operating Cell Temperature. All these data are commonly found in the manufacturer's standard information. Particular attention has been paid to the consideration of the dust and angle of incidence effects.

Some relevant aspects related to the design of the more important PV applications have been disclosed. It has been stressed that, whatever the detailed methodology, stand-alone PV-system sizing relies on future prediction (the expected system lifetime) based on past observations of the solar radiation data. The corresponding uncertainty, unavoidably associated with the random nature of the solar radiation, encompasses that simulation models can provide exact numbers but not automatically exact predictions. Concerning SHS, by far the most widespread PV application nowadays (in terms of the number of systems currently in operation), the difficulties for deriving representative standard energy consumption values have been pointed out. Finally, energy performance ratios for grid-connected PV systems have been defined.

ACKNOWLEDGEMENTS

Montse Rodrigo has been extremely kind in preparing all the figures. The comments of the editor have been extremely valuable. The writing of this chapter has been at the expense of many hours away from my loved ones. I must thank the large tolerance and patience of Leda and Cristina Celena.

REFERENCES

1. Serres M *et al.*, *Éléments d'Histoire des Sciences*, Chap. 3, Ed Bordas, Paris, 77–117 (1989).
2. Spencer J, *Search* **2**, 172–178 (1971).
3. Blanco M, Alarcón D, López T, Lara M, *Sol. Energy* **70**, 431–441 (2001).
4. Kasten F, *Arch. Meteorol. Geophys. Bioklimatol.* **14**, 206–223 (1966).

5. Meinel A, Mainel M, *Applied Solar Energy, An Introduction*, Addison-Wesley, Reading, MA (1976).
6. Iqbal M, *An Introduction to Solar Radiation*, Academic Press, Ontario (1983).
7. International H-World Database, *Mean Values of Solar Irradiation on Horizontal Surface*, Ed Progensa, Sevilla, Spain (1993).
8. SOLMET, *Solar Radiation-Surface Meteorological Observations*, National Climatic Data Center, TD-9724, Asheville, NC (1979).
9. Palz W, Greif J, *European Solar Radiation Atlas*, Commission of the European Communities, Ed Springer, Germany (1996).
10. Font Tullot I, *Atlas de la Radiación Solar en España*, Ed Instituto Nacional de Meteorología, Madrid, Spain (1984).
11. Capderou M, *Atlas Solaire de l'Algerie*, Ed EPAU, Alger (1985).
12. Colle S, Pereira E, *Atlas de Irradiação Solar do Brasil*, INM, Labsolar EMC-UFSC (1998).
13. *Atlas de radiació solar a Catalunya*, Institut Català d'Energia, Barcelona, Spain (1996).
14. NASA Surface Meteorology and Solar Energy Data Set. Available at eosweb.larc.nasa.gov/sse.
15. National Solar Radiation Data Base. Available at rredc.nrel.gov/solar.
16. Macagnan M, Lorenzo E, Jimenez C, *Int. J. Sol. Energy* **16**, 1–14 (1994).
17. Papoulis A, *Probability, Random Variables and Stochastic Processes*, McGraw-Hill, New York (1965).
18. Marion W, Urban K, *User's Manual for TMY2s*, Report to DOE DE-AC36-83CH10093, NREL (1995).
19. Liu B, Jordan R, *Sol. Energy* **4**, 1–19 (1960).
20. Page J, *Proc. U.N. Conf. New Sources Energy*, 378–390 (1961).
21. Collares-Pereira M, Rabl A, *Sol. Energy* **22**, 155–164 (1979).
22. Miguel A *et al.*, *Sol. Energy* **70**, 143–153 (2001).
23. Egidio M, Lorenzo E, *Sol. Energy Mater. Sol. Cells* **26**, 51–69 (1992).
24. Willier A, *Arch. Meteorol. Geophys. Bioklimatol.* **7**, 197–204 (1956).
25. Hopkinson R, *J. Opt. Soc. Am.* **44**, 455–459 (1954).
26. McArthur L, Hay J, *J. Appl. Meteorol.* **20**, 421–429 (1981).
27. Kondratyev K, *Radiation in the Atmosphere*, Academic Press, New York, NY (1969).
28. Hay J, McKay D, *Int. J. Sol. Energy* **3**, 203–240 (1985).
29. Perez R *et al.*, *Sol. Energy* **36**, 481–497 (1986).
30. Perez R *et al.*, *Sol. Energy* **39**, 221–231 (1987).
31. Siala F, Rosen M, Hooper F, *J. Sol. Energy Eng.* **112**, 102–109 (1990).
32. Standard ASHRAE 93-77, *Methods of Testing to Determine the Thermal Performance of Solar Collectors*, American Society of Heating, Refrigeration, and Air Conditioning Engineers, New York (1977).
33. Martin N, Ruiz J, *Sol. Energy Mater. Sol. Cells* **70**, 25–38 (2001).
34. Bottenberg W, “Module Performance Ratings: Tutorial on History and Industry Needs”, *PV Performance, Reliability and Standards Workshop*, 5–42, NREL, Vail, CO (1999).
35. Amato U *et al.*, *Sol. Energy* **37**, 179–194 (1986).
36. Graham V *et al.*, *Sol. Energy* **40**, 83–92 (1988).
37. Aguiar R, Collares-Pereira M, Conde J, *Sol. Energy* **40**, 269–279 (1988).
38. Benseman R, Cook F, *N Z J. Sci.* **12**, 296–708 (1960).
39. Lorenzo E, Maquedano C, *Proc. 13th Euro. Conf. Photovoltaic Solar Energy Conversion*, 2433–2436 (1995).
40. Quaschnig V, Hanitsch R, *Proc. 13th Euro. Conf. Photovoltaic Solar Energy Conversion*, 683–686 (1995).
41. Skiba M *et al.*, *Proc. 16th Euro. Conf. Photovoltaic Solar Energy Conversion*, 2402–2405 (2000).
42. Castro M *et al.*, *Era Sol.* **87**, 5–17 (1998).

43. Kaiser R, Reise C, *PV System Simulation Programmes*, Internal Report for the IEA SHCP Task 16, Fraunhofer-FISE, Freiburg (1996).
44. Caamaño E, Lorenzo E, *Prog. Photovolt.* **4**, 295–305 (1996).
45. Jennings C, Farmer B, Townsend T, Hutchinson P, Gough J, Shipman D, *Proc. 25th IEEE Photovoltaic Specialist Conf.*, 1513–1516 (1996).
46. Butti K, Perlin J, *A Golden Thread: 2500 Years of Solar Architecture and Technology*, Ed Cheshire, Palo Alto, NY (1980).
47. de Laquil III P., Kearney D, Geter M, Diver R, in Johansson T, Kelly H, Reddy A, Williams R, Eds, *Renewable Energy: Sources for Fuels and Electricity*, Chap. 5, Island Press, Washington, DC, 213–236 (1993).
48. Lorenzo E, Macagnan M, *Prog. Photovolt.* **2**, 45–55 (1994).
49. Zilles R, Ribeiro C, Moszkowicz M, *Proc. 2nd WCE Photovoltaic Solar Energy Conversion*, 2009–2012 (1998).
50. Durisch W, Tille D, Wörz A, Plapp W, *Appl. Energy* **65**, 273–284 (2000).
51. Eikelboom J, Jansen M, *Characterisation of PV Modules of New Generations*, ECN-C-00-067, Report to NOVEM Contract 146.230-016.1, Available at www.ecn.com (2000).
52. Caamaño E, Lorenzo E, Zilles R, *Prog. Photovolt.* **7**, 137–149 (1999).
53. Schmela M, *PHOTON Int.* **3-2001**, 32–35 (2001).
54. Green M, *Solar Cells*, Chap. 5, Prentice Hall, Kensington, 95–98 (1982).
55. Araujo G, Sánchez E, *Sol. Cells* **5**, 377–386 (1982).
56. King D, Kratochvil J, Boyson W, *Proc. 26th IEEE Photovoltaic Specialist Conf.*, 1113–1116 (1997).
57. Fuentes M, *Proc. 17th IEEE Photovoltaic Specialist Conf.*, 1341–1346 (1984).
58. Chianese D, Cerenghetti N, Rezzonico R, Travaglini G, *Proc. 16th Euro. Conf. Photovoltaic Solar Energy Conversion*, 2418–2421 (2000).
59. Scheiman D, Jenkins P, Brinker D, Appelbaum J, *Prog. Photovolt.* **4**, 117–127 (1996).
60. Smiley E, Stamenic L, Jones J, Stojanovic M, *Proc. 16th Euro. Euro. Conf. Photovoltaic Solar Energy Conversion*, 2002–2004 (2000).
61. Martin N, Ruiz J, *Prog. Photovolt.* **7**, 299–310 (1999).
62. Jones A, Underwood C, *Sol. Energy* **70**, 349–359 (2001).
63. King L, Kratochvil J, Boyson E, Bower W, *Proc. 2nd World Conf. Photovoltaic Solar Energy Conversion*, 1947–1952 (1998).
64. Gordon J, *Sol. Cells* **20**, 295–313 (1987).
65. Cowan W, *Proc. 12th Euro. Conf. Photovoltaic Solar Energy Conversion*, 403–407 (1994).
66. Abouzahr Y, Ramakumar R, *IEEE Trans. Energy Conversion* **5**(3), 445–452 (1990).
67. Negro E, *Proc. 13th Euro. Conf. Photovoltaic Solar Energy Conversion*, 687–690 (1995).
68. Kaiser R *Photovoltaic Systems*, Chap. Fraunhofer-FISE, Freiburg, Germany (1995).
69. Boland J, Marjolijn D, *Sol. Energy* **71**, 187–198 (2001).
70. Chapman R, *Sol. Energy* **43**, 71–76 (1989).
71. Macomber H, Ruzek I, Costello F, *Photovoltaic Stand-Alone Systems: Preliminary Engineering Design Handbook*, Prepared for NASA, Contract DEN 3-195 (1981).
72. Barra L, Catalanotti S, Fontana F, Lavorante F, *Sol. Energy* **33**, 509–514 (1984).
73. Bucciarelli L, *Sol. Energy* **32**, 205–209 (1984).
74. Bartoli B *et al.*, *Appl. Energy* **18**, 37–47 (1984).
75. Sidrach-de-Cardona M, Mora LI, *Sol. Energy Mater. Sol. Cells* **55**, 199–214 (1998).
76. Egido M, Lorenzo E, *Sol. Energy Mater. Sol. Cells* **26**, 51–69 (1992).
77. Klein S, Beckman W, *Sol. Energy* **39**, 499–512 (1987).
78. Lorenzo E, Narvarte L, *Prog. Photovolt.* **8**, 391–409 (2000).
79. Kaiser R, Sauer D, *Proc. 12th Euro. Conf. Photovoltaic Solar Energy Conversion*, 457–460 (1994).
80. Universal Technical Standard for Solar Home Systems, Thermie B SUP 995-96, EC-DGXVII (1998).

81. Maycock P, *Renewable Energy World* **2**, 72–76 (1999).
82. Nieuwenhout F *et al.*, *Prog. Photovolt.* **9**, 455–474 (2001).
83. Belli G, Iliceto A, Previ A, *Proc. 11th Euro. Conf. Photovoltaic Solar Energy Conversion*, 1571–1574 (1992).
84. Morante F, Zilles R, *Prog. Photovolt.* **9**, 379–388 (2001).
85. Jantsch M, Schmidt H, Schmid J, *Proc. 11th Euro. Conf. Photovoltaic Solar Energy Conversion*, 1589–1593 (1992).
86. *Guidelines for the Assessment of PV Plants. Document B: Analysis and Presentation of Monitoring Data*, Issue 4.1, JRC of the Commission of the European Communities, Ispra, Italy (1993).
87. Haeblerlin H, Beutler C, *Proc. 13th Euro. Conf. Photovoltaic Solar Energy Conversion*, 934–937 (1995).
88. Rindelhardt U, Teichmann G, Decker B, Grochowski J, *Proc. 14th Euro. Conf. Photovoltaic Solar Energy Conversion*, 2652–2655 (1997).
89. Katic Y, Jensen B, *Proc. 16th Euro. Conf. Photovoltaic Solar Energy Conversion*, 2830–2833 (2000).
90. Nofuentes G, *Contribución al desarrollo de aplicaciones fotovoltaicas en edificios*, Ph.D. thesis, Presented at the Polytechnical University of Madrid, Madrid (2001).
91. Mason N, Bruton T, Heasman K, *Proc. 14th Euro. Conf. Photovoltaic Solar Energy Conversion*, 2021–2024 (1997).
92. Wilk H, *Proc. 14th Euro. Conf. Photovoltaic Solar Energy Conversion*, 297–300 (1997).
93. Macagnan M, Lorenzo E, *Proc. 11th Euro. Conf. Photovoltaic Solar Energy Conversion*, 1167–1170 (1992).
94. Bourges B, *Climatic Data Handbook for Europe*, Ed Kluwer Academic Publishers, The Netherlands (1992).
95. Herrero M, *Soleamiento y Energía Solar*, Ed University of Valencia, Spain (1985).
96. PVSYST 3.1, www.pvsyst.com (2000).